The Report Committee for Neil Pankaj Shah
Certifies that this is the approved version of the following report

COMSOL Modeling of End Effects in Superhydrophobic Microchannels for Frictional Reduction

APPROVED BY
SUPERVISING COMMITTEE:

Supervisor:

Carlos H. Hidrovo

Mark Deinert

COMSOL Modeling of End Effects in Superhydrophobic Microchannels for Frictional Reduction

by

Neil Pankaj Shah, B.S

Report

Presented to the Faculty of the Graduate School of

The University of Texas at Austin

in Partial Fulfillment

of the Requirements

for the Degree of

Master of Science in Engineering

The University of Texas at Austin

August, 2010

Dedication

To my friends and family.

Acknowledgements

I'd like to thank Dr. Carlos Hidrovo for serving as my adviser and mentor throughout the course of my research. Special thanks are also in order for Dr. Deinert who served as my secondary reader. I'd also like to extend thanks to my lab mates in the Multiscale Thermal Fluids Lab (MTFL), specifically T.J Kim, Conan Zhang and Brian Carrol.

August 9th, 2010

Abstract

COMSOL Modeling of End Effects in Superhydrophobic Microchannels for Frictional Reduction

Neil Pankaj Shah, M.S.E.

The University of Texas at Austin, 2010

Supervisor: Carlos H. Hidrovo

This paper investigates the role of end-effects in superhydrophobic microchannels for frictional reduction through COMSOL based modeling. Two precursor derivations, the Kim & Hidrovo and Enright model are discussed and expanded upon through analytical and numerical simulations. The author performed numerical models on superhydrophobic microchannels with planar, stationary and finite separation distance of surface roughness element with perfect Cassie-Baxter air-layers. The simulations indicate an asymptotic limit for the flow-rate, indicating an optimum air-layer thickness. Numerical post processing reveals that this phenomenon is due to the recirculation end-effects that are relevant when the surface roughness separation distance is on order of magnitude of the channel width. These results are the first that identify end-effects as inducing a plateauing flow-rate and can serve as a benchmark for future studies.

Table of Contents

List of Tables

List of Figures

Chapter 1: Introduction

1.1 MOTIVATION

Advancements in the fabrication, design and synthesis of microscale structures have led to an increasing trend in the miniaturization of technology and processes [1]. For example, previous generations of integrated circuits and processors that once required centimeter lengths can now seamlessly be packed within mere millimeters. One technology that has received heavy research interest is the use of texturized microchannels to help transport and control fluids within microscale levels [2]. More specifically, the use of superhydrophobic microchannels shows potential due to its reduction in frictional forces versus conventional channels and therefore a firm understanding of their workings is critical for future microscale research.

Superhydrophobic microchannels and their frictional reduction properties show promise in a wide gamut of commercial, industry and research applications. Primarily they are ideal for small conduits or pipes with single or multiphase flow, specifically internal cooling for processors or other thermal-sensitive equipment. However there are possible opportunities that can extend beyond thermal management and instead to fluid regulation in BioMEMS chips [1], self-cleaning surfaces on solar panels, frost prevention on aircraft surfaces and microscale actuation of fluids [1, 3, 4]. Furthermore the technology behind superhydrophobic microchannels can be applied to external flow and can therefore result in applications in drag reduction on military aircraft, athletics or fuel savings for commercial

vehicles. With multitude of functions spanning across technical fields, an understanding of superhydrophobic microchannels is another driver in generating novel applications and advancing current knowledge.

1.2 EXPERIMENTAL LITERATURE REVIEW

Frictional reduction in channels was first observed in the early 1948 by Toms who experimented with turbulent flow within ducts that had modified surface properties, such as fibers or other wall features. Tom took experimental measurements of the pressure drop across the modified channels and found that the wall morphology helped stabilized eddies, vortices and other turbulent features and thus resulted in overall frictional reduction. However these results were limited to high Reynolds number and therefore did not explicitly translate to reducing frictional forces at lower laminar flow regimes [5].

Schnell (1956) was one of the earliest researchers to witness apparent slippage in water flow treated with dimethyldichlorosilane vapor and set the ground work for analytical models with slip boundary conditions within pressure driven systems [5]. Watannabe extended Tom's experiments to circular and non-circular ducts with a water-repellant or hydrophobic surface and was able to reduce drag within the laminar flow regime [6]. Furthermore, analysis of the Navier-Stokes equation and hot-wire anemometer velocity measurements concluded that contrary to conventional no-slip boundary conditions, the hydrophobic surface caused a slip condition at the wall and thus led to a slip velocity within the profile [7]. Specifically, the slip condition was only satisfied at low-flow rates and thus low Reynolds numbers,

giving additional evidence that laminar drag reduction potential could be exploited by altering the hydrophobicity of the surface [8].

While previous experiments were focused on relatively larger scale ducts and channels, the development of MEMS and other microscale techniques fueled interest in friction reduction on smaller scales during the early 21st century. Meinhart used micron scale velocimetry measurements on two microchannels; one coated with a hydrophilic glass layer and another with hydrophobic octadecyltrichlorosilane. Measurements revealed that while the hydrophilic microchannel fit the traditional no-slip boundary model, the hydrophobic microchannel instead had a wall velocity approximately 10% of the mean flow velocity—the first experimental evidence of a true slip velocity. In addition, Meinhart concluded that hydrophobic slip conditions were only applicable on lengths scale under 1 mm and therefore would be a significant component in microscale flows [9]. Further experiments with hydrophobic surfaces implied that the effective slip lengths were proportional to shear rates and were on orders of nanometers [10].

With material science and micro fabrication technologies advancing, it was possible to produce surfaces with variable roughness and surface features through nanolithography and etching of silicon surfaces [11]. Previous experiments focused on the role of solely uniform hydrophobic surfaces to achieve frictional reduction; with the ability to create features upon microscale surfaces, the impact of morphology on hydrophobicity could now be studied. Material scientists had long known that roughness and surface features impacted the hydrophobicity of a surface, as seen in nature through spherical water budding on the lotus flower [12]. Contact

angle experiments concluded that micropillars and other features could lead to superhydrophobic and ultrahydrophobic surfaces with contact angles in excess of 150°, well beyond the contact angles on solely smooth hydrophobic surfaces [10, 13-17].

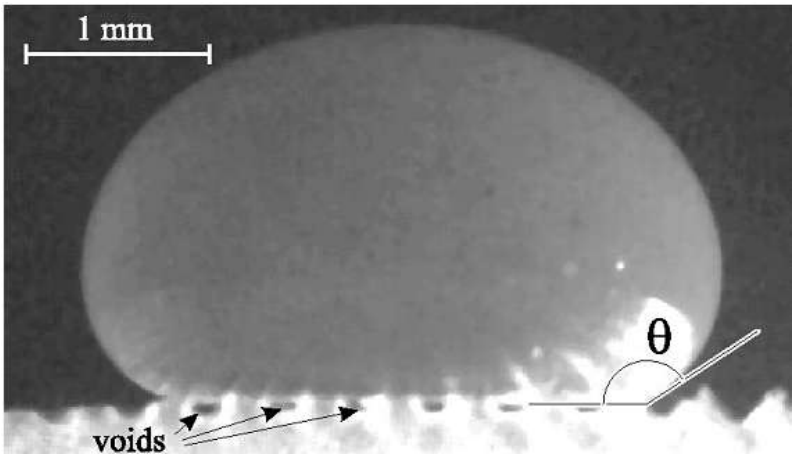

Figure 1.1: Higher contact angles achieved through microtextures [16]

Ou took previous experiments further by creating rough ultrahydrophobic microchannels flow cells and then measuring interface deflections via a confocal microscope and the pressure drop along the channel. Based on the curvature that occurred and friction reduction due to varying micropillar heights, Ou concluded that the trapping of air pockets between micropillars were primarily responsible for creating a shear-free layer and thus providing a possible source for the observed friction reduction [18, 19].

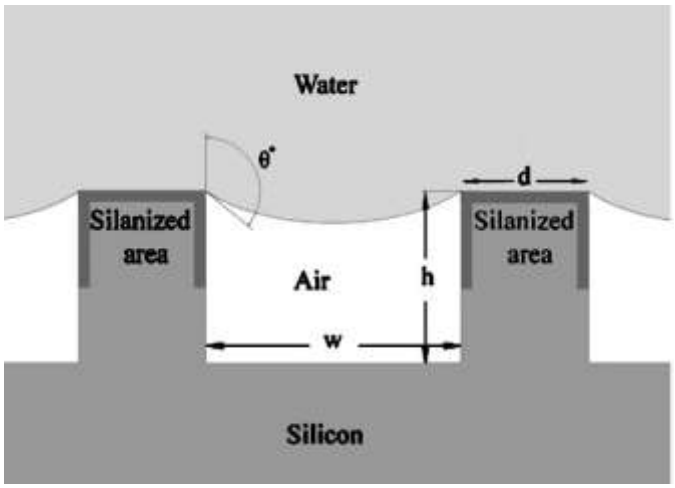

Figure 1.2: Proposed model for trapped air in microchannels [18]

The inclusion of trapped air for frictional reduction changed the traditional Navier-slip model—previous analytical models assumed a single phase system with slip boundary and slip velocity conditions [14]. Furthermore new experiments involving nanograte and other geometrically controlled features concluded that the transition from Wenzel to Cassie-Baxter state contributed to the shear-free layer and made frictional reduction possible [20-22]. Kim & Hidrovo developed a simple analytical model that governed stratified two phase flow with slip and a common pressure gradient [23]. Enright developed another multiphase flow model but incorporated far-end wall effects and individual pressure gradients for the water and air layers. The resultant yielded a flow-rate that exhibited asymptotic relation with respect to a growing air-layer. The Kim & Hidrovo and the Enright derivations are key precursors to the work of the report and as such, their underlying physics and implications will be discussed in a later chapter.

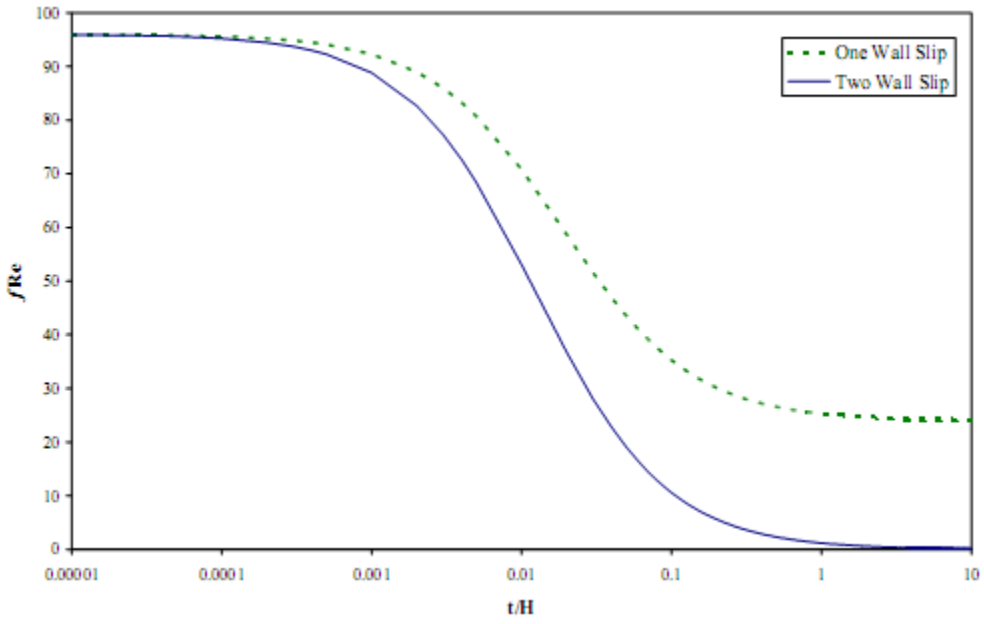

Figure 1.3: Enright model showing asymptotic behavior of flow rate [24]

Since previous experimental evidence points towards the Cassie-Baxter air layer as the source of lubrication, new research and focus has been around creating unique textures such as channels, ribs and micropillars and investigating the role geometry plays in maintaining the Cassie-Baxter state [2, 21, 23, 25-30].

1.3 COMPUTATIONAL LITERATURE REVIEW

Early computational studies on hydrophobic friction reduction lagged behind their experimental counterparts due to the limited computing power of the early 80's and 90s. Yet as processors and computer clusters became more sophisticated, computer simulations gained a rapid and ubiquitous prominence that is continued to this day.

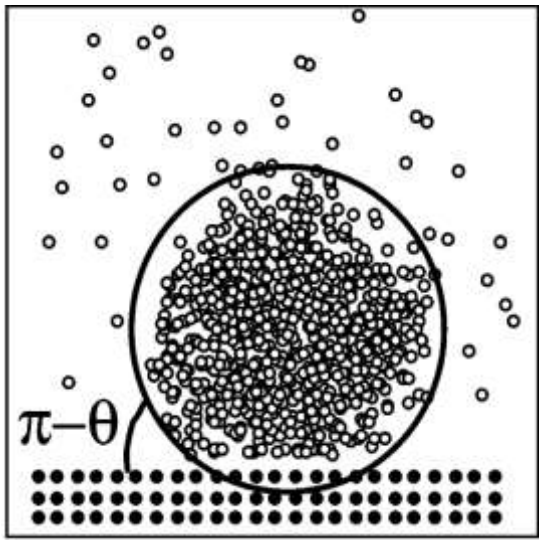

Figure 1.4: Bocquet MD simulation with contact angle [31]

The first numeric simulations were performed by Bocquet and Barrat, where they employed molecular dynamics (MD) simulations to model a droplet on a nanopore film. Unlike previous experiments, this simulation was unique in applying a finite contact angle to the droplet and thus resulting in an incomplete wetting state. The results indicated that slippage occurred on the film and specifically that the slip lengths were approximately 30 atomic diameters or 20 nanometers—greatly exceeding the pore height. Hence it was the first numerical evidence that indicated a slip boundary condition at low Knudsen numbers or at microscales [31]. Further simulations hinted that the slip length was dependent solely on the organization near the interface and did not have a direct dependency on flow conditions [32, 33].

Following a series of analytical experiments detailing that surface roughness plays a key role in hydrophobicity [10, 14, 16-19]; Barat extended the molecular

dynamics simulations to include non-uniform surfaces with microposts to provide a finite roughness. Their analysis showed that at low pressures a de-wetting transition to a superhydrophobic state occurred and that within this state slip lengths and velocities were significantly higher than that of a uniform hydrophobic surface. Similar to previous experiments with roughness, the simulations also confirmed that the surface roughness enhanced the hydrophobic nature of a material and that slip lengths increased accordingly. Bocquet proposed microchannel design parameters based on their numerically determined slip length and that the micropost height should be sufficient to tune capillary pressures for de-wetting transition [34].

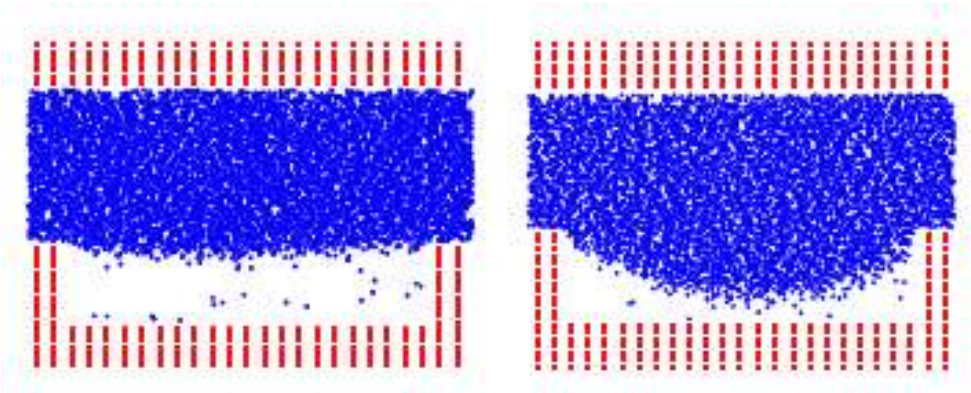

Figure 1.5: Barrat simulations showing de-wetting transition with pressure [34]

Since roughness was now numerically and experimentally determined to be an important factor in hydrophobicity and thus drag reduction, additional computational studies were centered on identifying parameters within a roughness profile. Kandlikar modeled the roughness as a saw-tooth pattern and identified the peak height, distance from mean line and spacing as parameters that defined the

overall roughness and thus the Moody friction factor [35]. Salamon utilized square pillar geometry in his numerical simulations and also included a shear-free air layer. He too found that the Navier-slip model sufficed for the bulk flow but broke down dramatically at the air-water interface and that ultimately a change in wetting state would greatly impact the slip-lengths [36].

Recently, computational analysis has been focused on assessing different roughness geometries as well as necessary pressures needed for Cassie-Baxter stability. Alternative modeling methods have also been proposed using a Lattice-Boltzmann model or a hybrid MD/Lattice-Boltzmann algorithm. The findings of these simulations confirm previous MD results and reinforce the notion that surface roughness and wetting conditions are key components of slip at small scales [37-41]. Commercial FEA solvers such as COMSOL have also been employed; Joshi studied transient behavior in microchannels and concluded that the cavity length was responsible for maintaining a confined air layer [2].

Figure 1.6: Joshi COMSOL study showing escaping air layer with large cavity lengths [2]

1.4 OBJECTIVES AND SCOPE OF STUDY

The current microchannel research landscape is ripe with analytical models concerning multiphase flow and computational studies focused on slip flow. Past experiments and simulations have concluded that superhydrophobic microchannels can reduce friction through the inclusion of roughness features that confine air cavities. However previous research have been limited in scope and focused on the individual constituents that make up hydrophobic slip flow, such as the surface elements or multi-phase flow. There have not been any studies to assess the combined effects of surface roughness elements, repeated cavities and slip flow, specifically for typical length scales seen in the lab.

The objective of this report was to use COMSOL simulations to investigate the role of cavity geometry plays on the flow-rate and frictional reduction in realistic microchannels. For simplicity the author ignored Cassie-Baxter to Wenzel transition and other wetting effects but included wall effects. The resultant computational studies on superhydrophobic microchannels indicate that the combined effects of walls and air-recirculation caused a limited terminal flow-rate through the microchannel. These new results provide a new ceiling on microchannel friction reduction and can serve as a valid benchmark for future studies and design optimization.

Chapter 2: Background Theory

2.1 Microscale Fluid-Dynamics and Hydrophobicity

It is widely accepted that microchannels are flow conduits that have diameters less than 1 millimeter and typically have features on order of microns [28] . At this scale the Reynolds number is typically low and the applied flows are expected to be within the laminar regime, though turbulence and transition is possible [42]. Since the length scales in microchannels are quite small and pressure drop scales with $1/H^3$ with respect to the channel height, there are severe limitations to internal flow rates due to frictional losses [13].

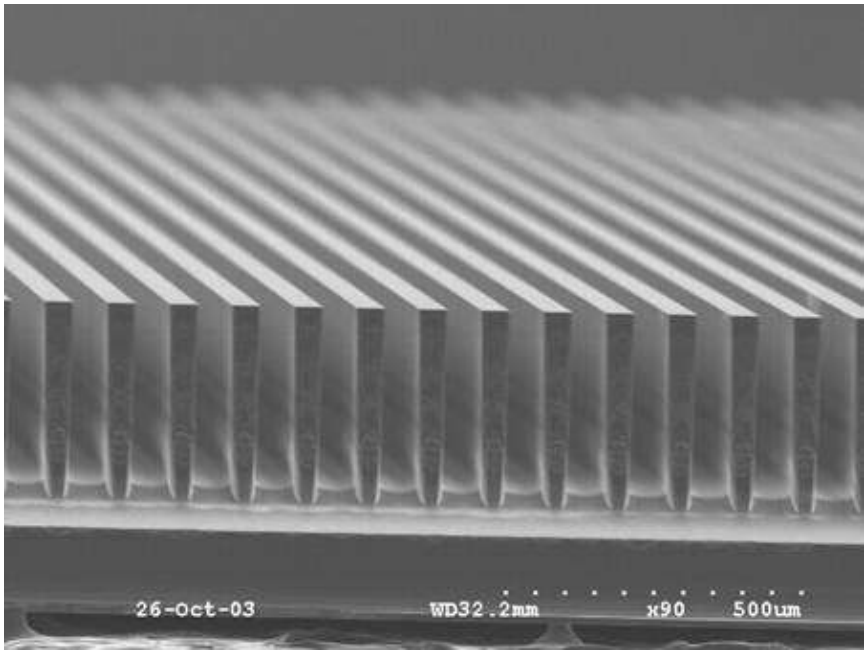

Figure 2.1: 500 micrometer microchannel [43]

Engineers and researchers have conceptualized or devised different technologies to try to circumvent the pressure-drop issues at the microscale—for example the use of small micro-pumps to overcome frictional head. While micro-pumps provide sufficient head to maintain flow-rate through microchannels, they are often composed of numerous parts and hence add complexity and time to the fabrication process. [3] However an alternative method to reduce frictional losses has been through the novel modification of microchannel surfaces and features [7]. By using hydrophobic materials in conjunction with micro-textured patterns within the microchannels, researchers have been able to induce phenomena called super hydrophobicity.

Superhydrophobicity is the ability for a wetting fluid, specifically water, to maintain a thermodynamically stable contact angle greater than 150°. This equilibrium contact angle, which ranges from 0° for perfect wetting to 180° for perfect non-wetting, is determined by the classical Young relation [44].

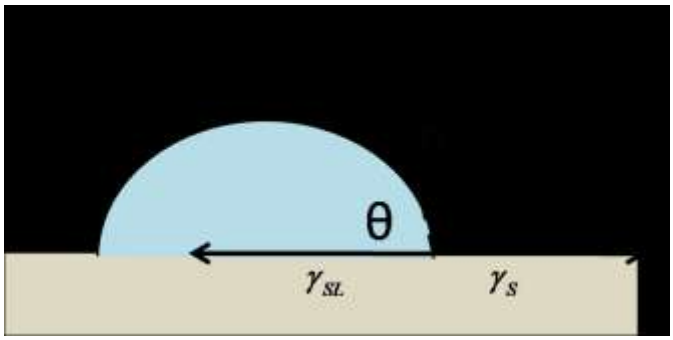

Figure 2.2: Ideal wetting via Young's model

$$\gamma_{SL} = \gamma_S - \gamma_L \cos(\theta) \tag{0.1}$$

Here the surface energy of the solid-gas, liquid-gas and the solid-liquid are represented by γ_s, γ_L and γ_{SL} accordingly, and the equilibrium Young's angle is denoted as θ [44]. Looking at the Young's relation, the overall wetting angle θ is contingent upon the different phase interfacial energy—therefore changing this solid-liquid energy by changing the surface material is one way to modify the contact angle. Analogous to how rain-coats are made of material with low interfacial energy and therefore force water droplets into a de-wetting orientation, researchers have identified various materials that possess hydrophobic de-wetting or the opposite, hydrophilic properties. In nature, lotus blossom leaves have been known for their water budding or lotus effect [12] and within the medical and research realm, the organosilicon PDMS is a synthetic compound that promotes hydrophobicity[9].

While the Young's relation is the classical and fundamental equation that determines the overall contact angle between a wetting-fluid and a surface, it assumes an ideal surface with no innate roughness. SEM microscopy measurements have revealed that most surfaces exhibit some sort of finite roughness and therefore deviate from the ideal Young's equation. Instead, in real-world applications with rough surfaces, there are two dominating wetting regimes that can exist within a wetting system; the Wenzel state and the Cassie-Baxter state.

The Wenzel state describes a single fluid that fully penetrates the roughness features on a surface, as seen in figure 1.2, and now forms a new equilibrium contact angle, θ_w, with the surface. This phenomenon was first noted by Wenzel and represented by the Wenzel relation(0.2).

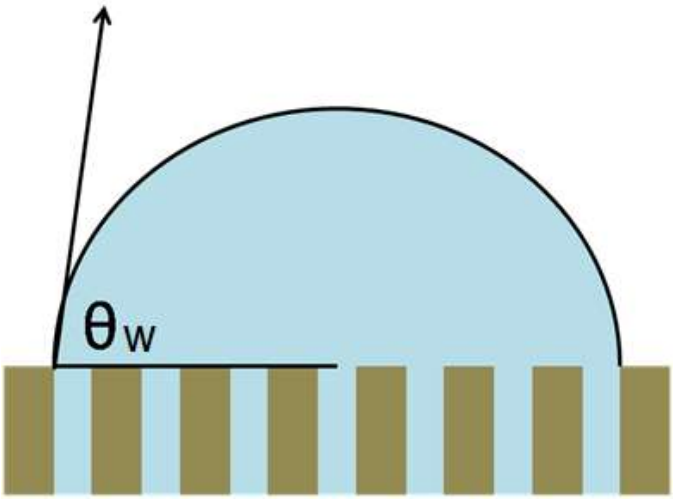

Figure 2.3: Wenzel wetting of homogenous fluid on a rough surface

$$\cos(\theta_w) = r\cos(\theta) \tag{0.2}$$

In the Wenzel relation, r represents the ratio of surface-contact area to apparent area of the rough features and θ was the previous Young's contact angle [45]. From the relation the importance of the surface roughness is evident; within the Wenzel equation--the surface roughness can amplify or dampen the overall equilibrium Young's contact angle.

While the Wenzel model represents a homogenous wetting state another possible situation can occur when two fluids interact heterogeneously with a rough surface, producing the Cassie-Baxter state. In this state the wetting liquid is suspended above another fluid that penetrates the rough features and thus forms a new contact angle θ_{CB}. The relationship between the new Cassie-Baxter contact

angle and the previous Young's contact angle is defined by the Cassie-Baxter relation(0.3).

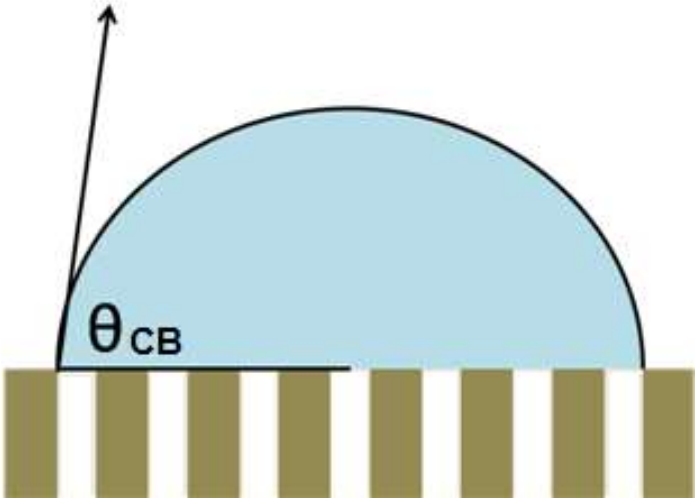

Figure 2.4: Cassie-Baxter wetting with water and full air penetration

$$\cos(\theta_{CB}) = \phi(\cos\theta + 1) - 1 \qquad (0.3)$$

Here ϕ is the area fraction, contact over total area, in which the suspended wetting fluid is in contact with the rough features [46]. This contact area is a function of the contact geometry of the rough elements and similar to the Wenzel equation, it can dramatically change the contact angle of the wetting fluid. It is this particular feature that allows for the ability to maintain superhydrophobic states with contact angles well beyond conventional smooth surface limits.

The Cassie-Baxter state is typically less stable than the Wenzel state and can only be maintained under a critical pressure which is based on the Laplace and capillary pressures of the water-air interface. Beyond this capillary pressure the air

layer can't be maintained and transition to Wenzel occurs. While the exact mechanism of Cassie-Baxter to Wenzel transition is still unknown, researchers have identified pressure and roughness morphology as key parameters for maintaining a specific state. In some models the air-layer pressure contributes a spring-like compressibility effect and therefore has an energy threshold required before transition occurs. Recently, it has been shown that the wetting transition from Cassie-Baxter to Wenzel can be reversed by re-pressurizing the air-layer. [21, 47-52]. Liquids that experience Cassie-Baxter wetting are typically much more mobile than their Wenzel counterparts due to contact with the air free-shear layer [53]. This mobility can be exploited in textured superhydrophobic microchannels where the high contact angle allows for a two-phase system of water suspended upon pockets of air.

2.2 MICROCHANNEL SLIP-THEORY

The traditional no-slip boundary condition is empirical in nature but at small length scales it can break down allowing slip-flow to occur at boundaries or interfaces [7]. Slip flow is a specific case in which a fluid interface has a finite interfacial velocity, or u_{slip} at a boundary, as opposed to zero in the no-slip case. It is important to note that fluids typically have some sort of slippage at the boundary but the relevance of the slippage on the overall fluid-physics is contingent upon the length scale of the overall system. Determination of when slip is relevant is probed through the non-dimensional parameter the Knudsen number Kn, which is the ratio

of the mean free path λ and the characteristic length scale L of the system. The Knudsen number provides a barometer to gauge whether individual statistical mechanics or continuum mechanics are appropriate in analyzing the system; for low Knudsen numbers below 10^{-2} the entire flow can be treated as a continuum while values above 10 require statistical mechanics to account for atomic interactions [37].

$$Kn = \frac{\lambda}{L} \tag{0.4}$$

For Knudsen numbers between 10^{-2} and 0.1 which corresponds to typical microchannel scales, slip flow becomes relevant. The slip velocity that occurs at the interface u_{slip} is commonly modeled to the interfacial shear stress through a mathematical construct called the Navier slip length(0.5).

$$u_{slip} = b \left. \frac{du}{dy} \right|_{wall} \tag{0.5}$$

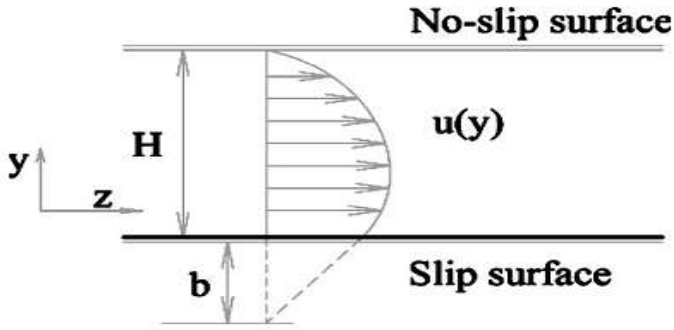

Figure 2.5: Slip flow with slip boundary [24]

The slip length b is the extrapolation of the linearized velocity profile extending to some length below the slip-plane where the hypothetical velocity would be 0. The slip length can also be expressed as a function of the shear stress acting upon the wall through the definition of shear stress at the wall, where

$$\tau_w = \mu \frac{du}{dy} \tag{0.6}$$

Combining equation (0.5) and (0.6) allows for the slip length b to be expressed as

$$b = \frac{u_{slip}\mu}{\tau_w} \tag{0.7}$$

For flow between parallel plates the overall flow-rate can be derived analytically from the Navier-Stokes equation.

Figure 2.6: Parallel plate geometry

Assuming fully developed flow, the 2-D Navier-Stokes equations reduces to (0.8) where u is the y-directional velocity, μ is the fluid viscosity and $\frac{dp}{dx}$ is the x-directional pressure gradient.

$$\frac{d^2u}{dy^2} = \frac{1}{\mu}\left(\frac{dp}{dx}\right) \tag{0.8}$$

Integration of this reduced Navier-Stokes equation (0.8) yields the following velocity expression with two subsequent integration constants.

$$u = \frac{1}{\mu}\left(\frac{dP}{dx}\right)\frac{y^2}{2} + C_1 y + C_2 \tag{0.9}$$

Under traditional no slip boundary conditions the velocity is 0 at both walls.

$$\text{u =0 at } y = \pm\frac{H}{2} \tag{0.10}$$

Applying the boundary condition and solving for integration constants will yield the well-known Hagen-Poiseuille solution for flow between infinite parallel plates with the following velocity profile u(y) and bulk velocity, U [54].

$$u = \frac{3}{2}U\left[1 - \left(\frac{y}{H/2}\right)^2\right] \tag{0.11}$$

$$U = \frac{H^2}{12\mu}\left(-\frac{dP}{dX}\right) \tag{0.12}$$

In general the flow rate Q is typically an important engineering parameter, particularly for sizing pump systems or characterizing flow performance in an experiment. The flow rate Q can be found through integration of the velocity profile over the corresponding cross-sectional area.

$$Q = \int_{0}^{w} \int_{-\frac{H}{2}}^{\frac{H}{2}} u(y) dy \tag{0.13}$$

Upon substituting (0.11) and(0.12), equation (0.13) yields the flow rate per unit width.

$$\frac{Q}{w} = -\frac{H^3}{12\mu}\left(\frac{dP}{dx}\right) \tag{0.14}$$

In most conditions, the cross sectional area of a channel will remain constant and the operating fluid can be assumed incompressible and therefore allowing the pressure drop to be related directly to the length of the channel L.

$$\left(\frac{dP}{dx}\right) = \frac{\Delta P}{L} \tag{0.15}$$

Ultimately this reduces the flow rate expression (0.14) to the following.

$$\frac{Q}{w} = \frac{H^3}{12\mu}\frac{\Delta P}{L} \tag{0.16}$$

If the overall system's length scale is reduced such that its Knudsen number is between .001 and, 01, slip flow can now play an important role. Referring back to the previous geometry, we can now apply slip boundary conditions (0.17) to replace the previous no-slip boundary conditions(0.10).

$$\begin{aligned} u &= u_{slip} \\ y &= \pm\frac{H}{2} \end{aligned} \tag{0.17}$$

Applying slip boundary conditions (0.17) to (0.9) and then arithmetically solving for the integration constants will yield the overall slip flow velocity profile(0.18).

$$u(y) = u_{slip} - \frac{H^2}{8\mu}\frac{dP}{dx}\left[1 - \left(\frac{y}{H/2}\right)^2\right] \tag{0.18}$$

Once again the flow rate Q is typically sought and can be found through integration along the cross-sectional area.

$$\frac{Q_{slip}}{w} = u_{slip}H - \frac{H^3}{12\mu}\left(\frac{dP}{dx}\right) \tag{0.19}$$

Assuming incompressible flow and constant cross sectional area from(0.15), (0.19) can be presented as:

$$\frac{Q_{slip}}{w} = u_{slip}H + \frac{H^3\Delta P}{12\mu L} \tag{0.20}$$

The form of equation 1.19 is very similar to the no-slip flow rate equation of 1.13—the profile exhibits the expected parabolic dependency on channel height and pressure gradient but the inclusion of the slip flow adds a plug flow component.

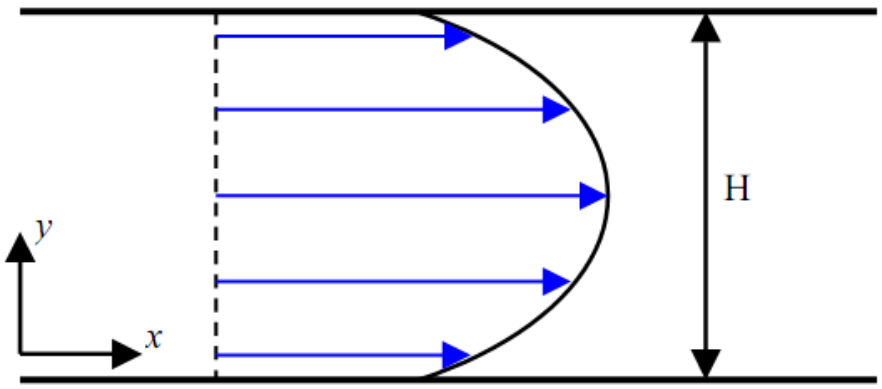

Figure 2.7: Double wall slip flow [16]

The flow rate can also be expressed as function of slip length through the slip velocity in (0.5) and the overall velocity profile (0.18) .The velocity gradient at the wall can be expressed by differentiating the velocity profile.

$$\left.\frac{du}{dy}\right|_{wall} = -\frac{H^2}{4\mu}\frac{dP}{dx}\left[-\frac{2y}{H}\right]_{-\frac{H}{2}} = -\frac{H}{2\mu}\frac{dP}{dx} \tag{0.21}$$

Substitution of the velocity gradient and slip length into (0.18) will now give the velocity profile as a function of slip length b.

$$u(y) = \frac{b\Delta p}{\mu L} + \frac{H^2\Delta p}{4\mu L}\left[1-\left(\frac{y}{H/2}\right)^2\right] \tag{0.22}$$

Once again the velocity profile can be integrated over its corresponding cross-section area to get the flow-rate per unit width.

$$\frac{Q_{slip}}{w} = \frac{2bh^2\Delta P}{\mu L} + \frac{2h^3\Delta P}{3\mu L} \tag{0.23}$$

Now in the case of single-wall slip with the following modified boundary conditions:

$$\begin{aligned} u &= 0 \text{ at } y = \frac{H}{2} \\ u &= u_{slip} \text{ at } y = -\frac{H}{2} \end{aligned} \tag{0.24}$$

Equation (0.9) can be solved arithmetically to yield the following.

$$u(y) = \frac{u_{slip}}{2} - \frac{u_{slip}y}{2H} + \left(\frac{dP}{dx}\right)\frac{H^2}{8\mu}\left(1 - \left(\frac{y}{H}\right)^2\right) \tag{0.25}$$

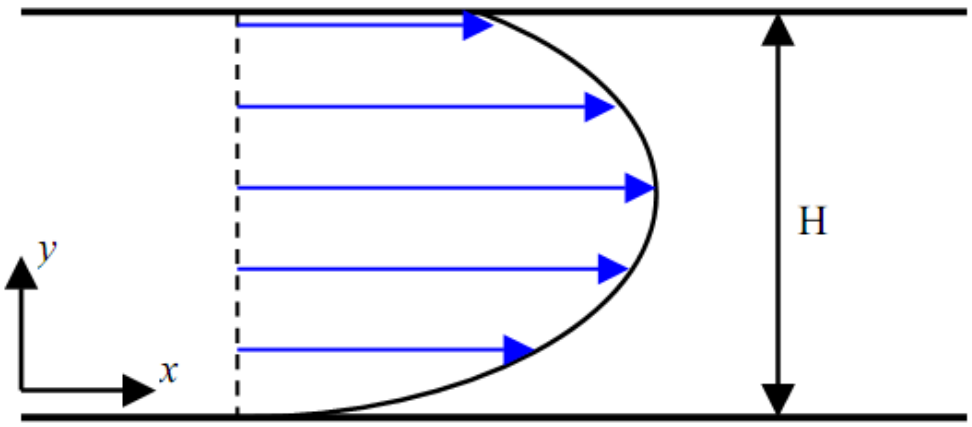

Figure 2.8: Single wall slip flow [16]

Following the previous examples, the flow rate can be found as:

$$\frac{Q_{slip}}{w} = \frac{u_{slip}H}{2} + \frac{H^3}{12\mu}\left(\frac{dP}{dx}\right) \tag{0.26}$$

Or

$$\frac{Q_{slip}}{w} = \frac{u_{slip}H}{2} + \frac{H^3}{12\mu}\left(\frac{\Delta P}{L}\right) \tag{0.27}$$

In summary slip flow is a specific case in which the no-slip boundary condition is replaced by a velocity, similar to a sliding wall. Slip flow is relevant in microchannels since the characteristic length scale is on order of the mean free path which is commonly expressed as the Knudsen number(0.4). Due to the existence of a slip-velocity at the boundary, microchannels with slip typically have higher flow rates than their non-slip counterparts. Furthermore the overall flow-rate through the system is heavily dependent on the slip velocity. The ability for superhydrophobic microchannels to have a slip velocity and hence exhibit slip flow is key to the following derivations and computational study, and serve as the basis of hydrophobic microchannel research.

Chapter 3: Analytical Models

3.1 KIM & HIDROVO TWO-FLUID DERIVATION

The previous section's equations and expressions were derived by assuming a single phase fluid with slip boundary conditions. However in most microchannels that operate within the Cassie-Baxter regime, the system consists of two fluids, typically water and air, with a slip boundary condition. Kim & Hidrovo presented a simple derivation for a two-phase system of water and air with slip flow. [23] Furthermore they assumed that the water and air layers shared a common pressure gradient and there were no textured or surface roughness elements. The derivation is graphically represented in Figure 3.1, with an air thickness h_{air}, water thickness h_{water} and interfacial slip velocity u_{slip} at y=0.

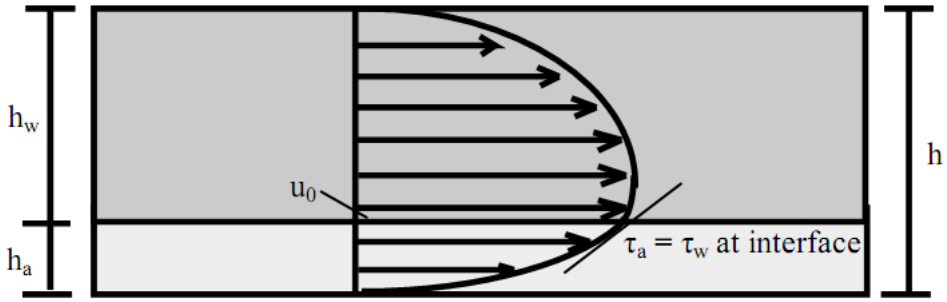

Figure 3.1: Two-phase flow of water and air with slip [34]

The Navier-Stokes equations (0.8) are now subjected to the following boundary conditions. .

$$\begin{aligned} u &= u_{slip} \text{ at } y = 0 \\ u &= 0 \text{ at } y = h_{water} \\ u &= 0 \text{ at } y = h_{air} \end{aligned} \tag{0.28}$$

Substituting the boundary conditions (0.28) into the integrated Navier-Stokes equations (0.9) yields the velocity profiles for the water(0.29) and air layers (0.30) respectively .

$$u_{water} = \frac{y^2}{2\mu_{water}}\frac{dp}{dx} + \left(\frac{h_1}{2\mu_{water}}\frac{dp}{dx} + \frac{u_{slip}}{h_1} \right) y + u_{slip} \tag{0.29}$$

$$u_{air} = \frac{y^2}{2\mu_{air}}\frac{dp}{dx} - \left(\frac{h_2}{2\mu_{air}}\frac{dp}{dx} + \frac{u_{slip}}{h_2} \right) y + u_{slip} \tag{0.30}$$

The effectual slip velocity can also be found by continuity of shear stresses at the interface(0.31),

$$\tau_{water} = \tau_{air} \text{ at } y = 0 \tag{0.31}$$

Yielding the following expression for u_{slip} .

$$u_{slip} = -\frac{1}{2}\frac{dp}{dx}\frac{h_{water}h_{air}(h_{air} + h_{water})}{\mu_{water}h_{air} + \mu_{air}h_{water}} \tag{0.32}$$

Since water is the operating fluid within microchannels, its flow rate is of primary concern and can be found by integration of the water profile(0.29).

$$\frac{Q_{water}}{w} = \frac{h_{water}^{\ 2}}{4}\left(-\frac{dP}{dx}\right)\frac{h_{water}}{3\mu_{water}} + \frac{h_{air}\left(h_{air}+h_{water}\right)}{\mu_{air}h_{water}+\mu_{water}h_{air}} \tag{0.33}$$

3.2 NON-DIMENSIONAL PARAMETERIZATION

In order to compare different derivations and models together, it is common to use generalized non-dimensional parameters. These terms will scale the relevant factors, such as air-layer thickness or flow-rate, across the models and provide a general benchmark for comparison. The first parameter employed is h^* which is the ratio of the air thickness layer to the water layer.

$$h^* = \frac{h_{air}}{h_{water}} \tag{0.34}$$

h^* parameterizes the interface and allows for comparisons for shallower or deeper channels. Hence a higher h* value indicates that the individual air-filled pockets are much larger than the height of their water channel counterparts. The water flow rate Q can be non-dimensionalized through Q^* as shown below.

$$Q^* = \frac{Q\mu_{water}}{\frac{dP}{dx}h_w^{\ 4}} \tag{0.35}$$

Q^* also has a more intuitive meaning that is related back to the Poiseuille number which is defined specifically for a square duct:

$$Po = f\,\mathrm{Re} = \frac{2D_H^{\,2}}{\mu\left(\frac{Q}{A}\right)}\frac{dP}{dx} \tag{0.36}$$

The hydraulic diameter D_h is defined as twice the height of the microchannel or 2*h_w and assuming that the width is the same as the channel height (0.36)can be rewritten as:

$$Po = f\,\mathrm{Re} = \frac{2(2*h_w)^2}{\mu\left(\frac{Q}{h_w^{\,2}}\right)}\frac{dP}{dx} \tag{0.37}$$

Upon simplifying (0.37) yields the following expression.

$$Po = f\,\mathrm{Re} = \frac{8\,h_w^{\,4}}{\mu\,\mathrm{Q}}\frac{dP}{dx} \tag{0.38}$$

Now making use of the non-dimensional parameter Q^*, (0.38) can be finally rewritten as the following.

$$Po = f\,\mathrm{Re} = \frac{8}{Q^*} \tag{0.39}$$

Thus looking at (0.39) reveals that Q* is inversely related to the Poiseuille number of the microchannel and hence the frictional losses. It is important to note that this particular derivation is specific to a square channel duct--however the key conclusion is that the Q* parameter is inversely related to the Poiseuille number and can serve as a proxy for friction factor and ultimately frictional reduction in a microchannel. Following the preceding examples, the interfacial slip velocity can be non-dimensionalized as follows.

$$U^* = \frac{u_{slip}\mu_{water}}{\frac{dP}{dx}h_w^{\,2}} \tag{0.40}$$

The previously defined non-dimensional terms will be used to parameterize the derivations and models discusses in this study and to sequester the effects of different geometric configurations from the flow physics.

3.3 KIM & HIDROVO RESULTS

The previous flow-rate and slip-velocity can now be expressed as function of the non-dimensional parameters, as seen in figures 3.2 and 3.3 respectively. The first observation is that both plots have similar trends--a region of rapid increase at low h* values which leads to a linear and unbounded relation between Q* and u* with h*. It is expected that both charts have similar trends and characteristics due to the relationship between flow -rate and slip-velocity. From(0.27), it can be seen that the overall flow-rate of a single wall slip system is a combination of the normal pressure driven flow and a slip-velocity plug form. Hence, the slip velocity is the main driving force behind flow within the microchannel and the trends should be similar.

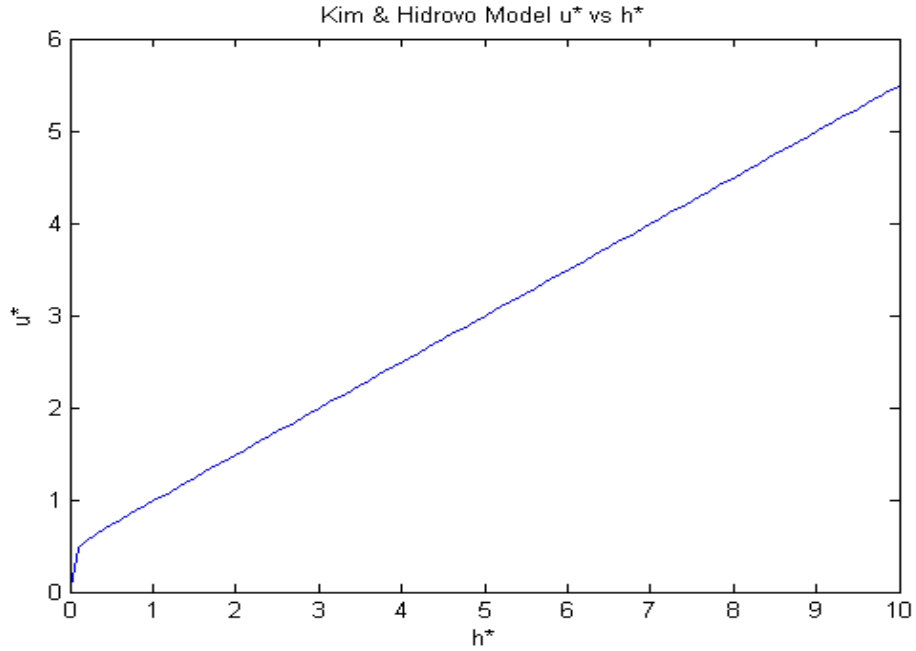

Figure 3.2: u* vs. h* for Kim & Hidrovo model

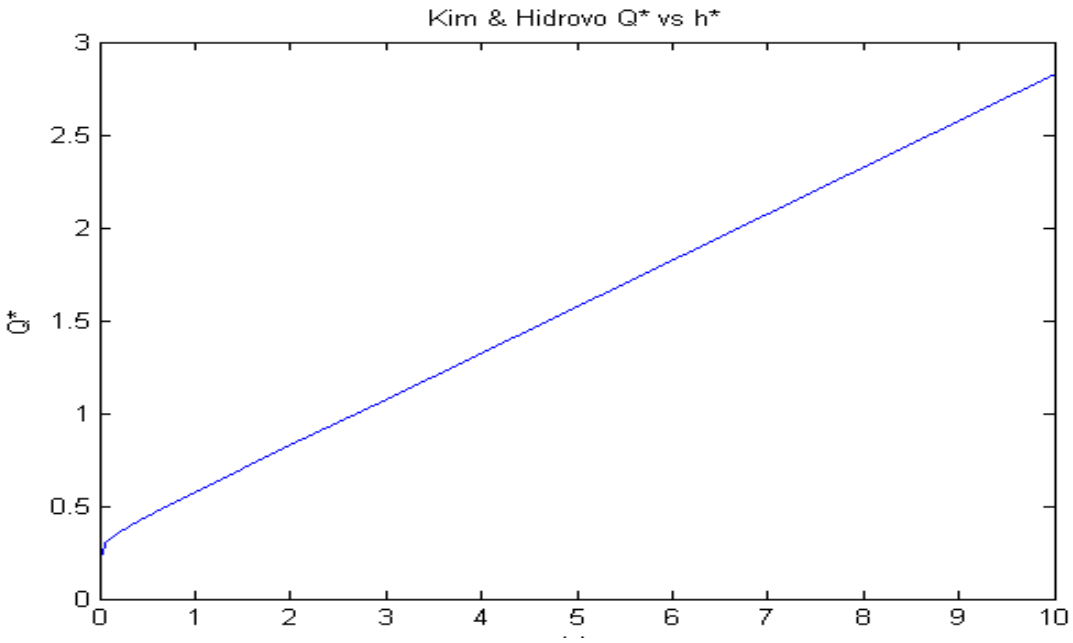

Figure 3.3: Q* vs. h* for Kim & Hidrovo Model

The existence two different regimes within this model can be understood by first analyzing the following non-dimensional interfacial shear stress versus h* plot.

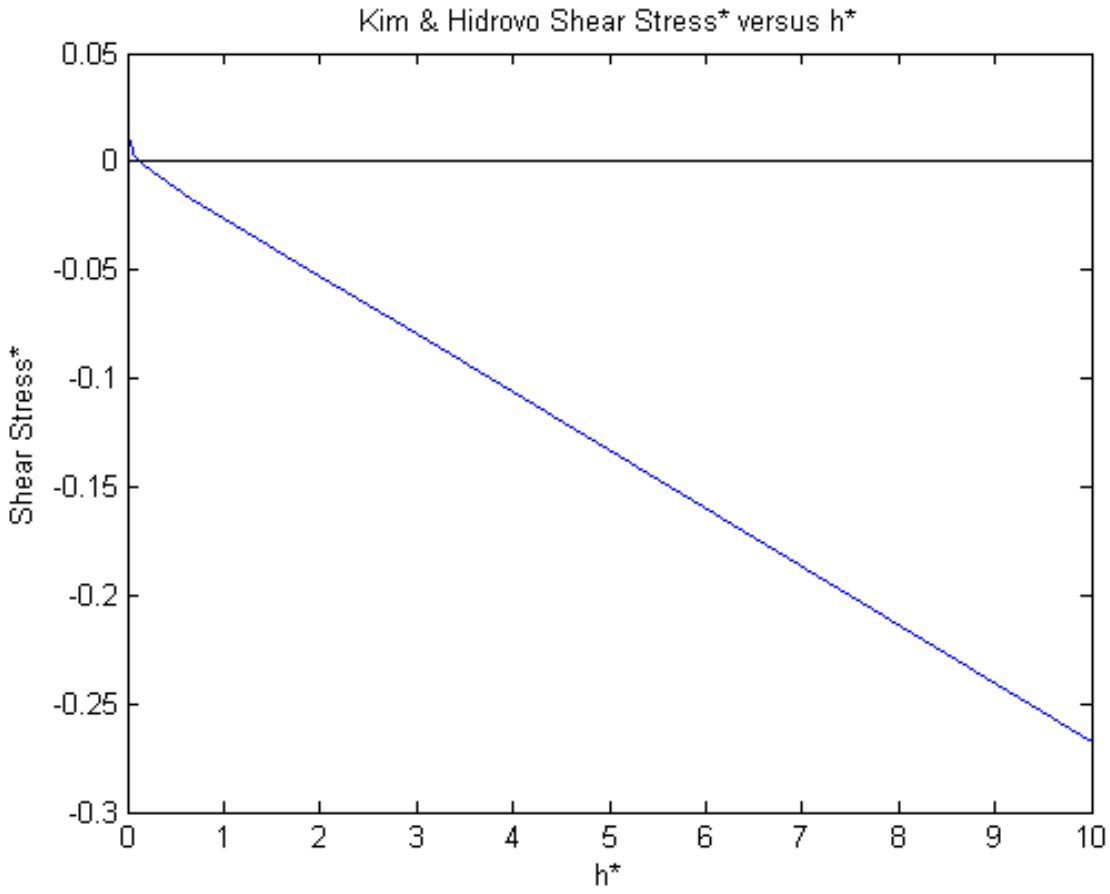

Figure 3.4: Non-dimensional shear-stress vs. h*

Zooming in specifically on the previous figure reveals that the interface shear stress changes signs at a critical h* value. Since the shear stress represents the velocity gradient, this change of signs represents a change in slope of the velocity at the interface.

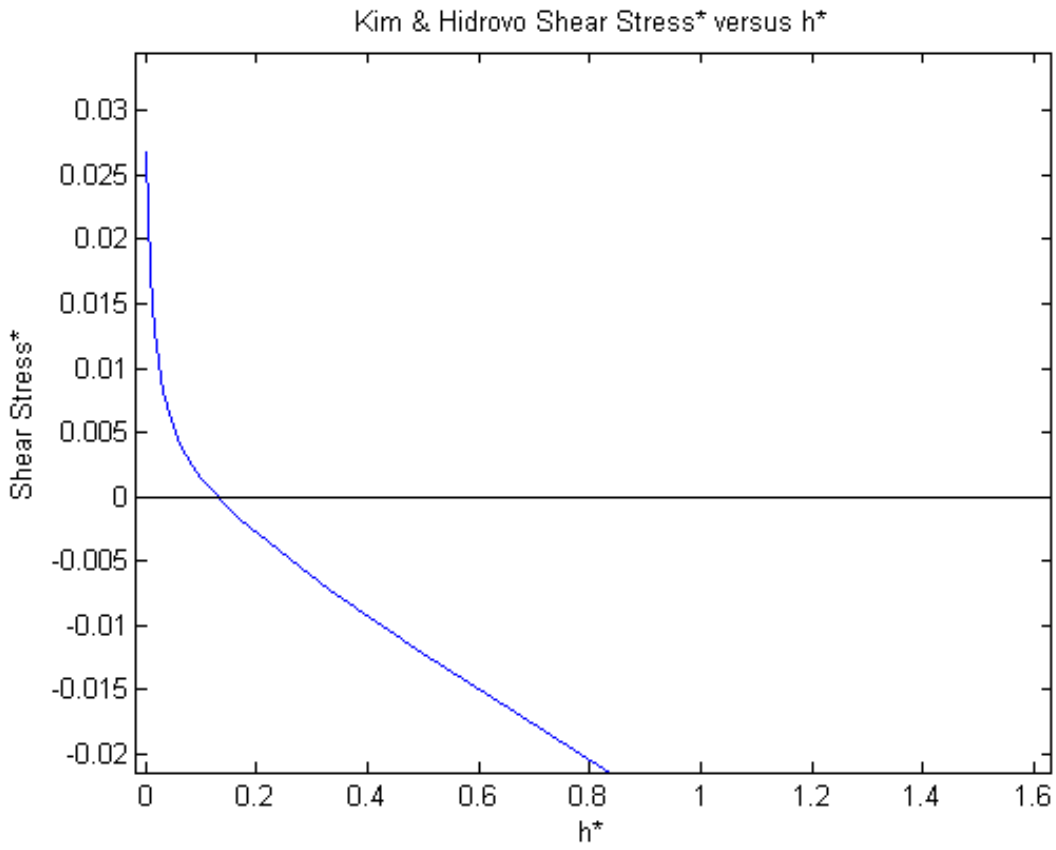

Figure 3.5: Zoomed in plot showing shear stress sign change

This change in shear stress signs gives rise to two distinct regions within the multiphase model that are analogous to a balance between Poiseuille or pressure driven flow and Couette, or a sliding wall flow. At low h* values the microchannel depth is dominated by the water channel's height and hence there is a very thin air-layer. While there is slip at the interface at finite and low h* values due to the existence of an air layer, the air layer is very thin and instead the water centerline velocity exceeds the interfacial slip velocity. The resultant is a dominant Poiseuille condition with minimum slip at the interface with a velocity profile as depicted in the

following figure. This primary Poiseuille driven water flow gives rise to the first regime seen in figure 3.2 and figure 3.3.

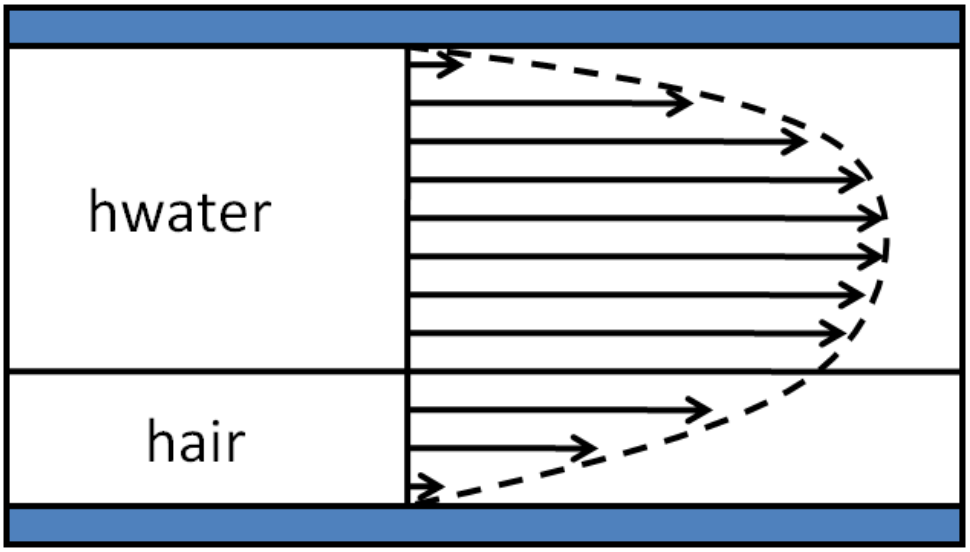

Figure 3.6: Poiuselle dominated flow (regime 1) for low h*

However once a critical h* is reached the air layer will have a higher average velocity than the water component that stems from its much lower viscosity under the same shared pressure gradient. Hence the interfacial velocity will be higher than the water's average velocity and the interface will exhibit a higher degree of slip. This can be likened to a shift away from the previous Poiseuille pressure driven flow and instead to a sliding wall Couette flow condition.

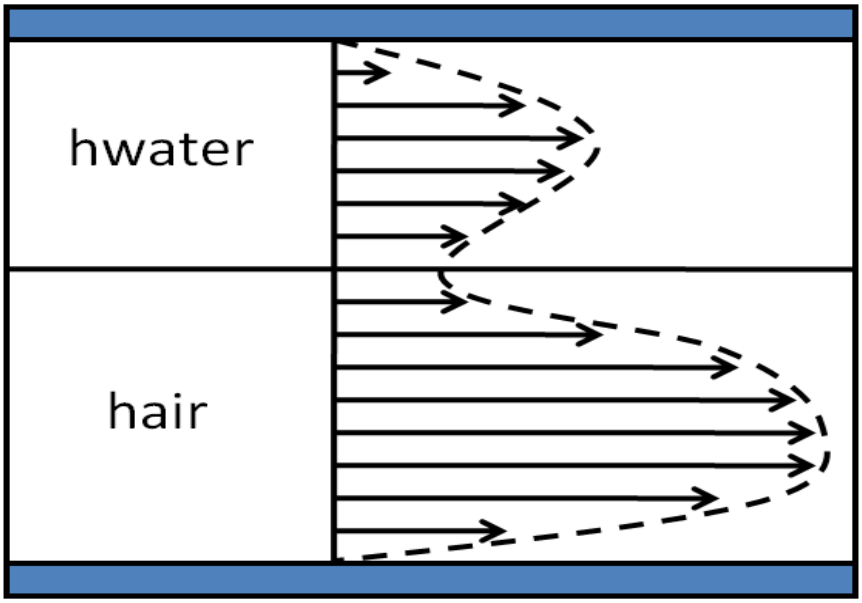

Figure 3.7: Couette dominating flow (regime 2) for higher h*

In the high h* case, the air layer is dominating the flow profile of the microchannel and this higher velocity translates to a higher interfacial slip velocity. Analogous to the Couette driven flow, the water-flow is now being dragged or driven by the higher speed air-flow and its interfacial velocity. Naturally the interfacial velocity will therefore be unbounded after this critical h* and as h* grows larger, the overall water flow rate will follow, explaining the 2nd regime within figure 3.2 and figure 3.3.

Figure 3.8 shows Q* and the shear stress normalized by their maximum values and plotted as a function of h*.From the plot, the necking transition from the Poiseuille dominated regime to Couette dominated regime 2 occurs at the same critical h* in which the shear stress changes signs.

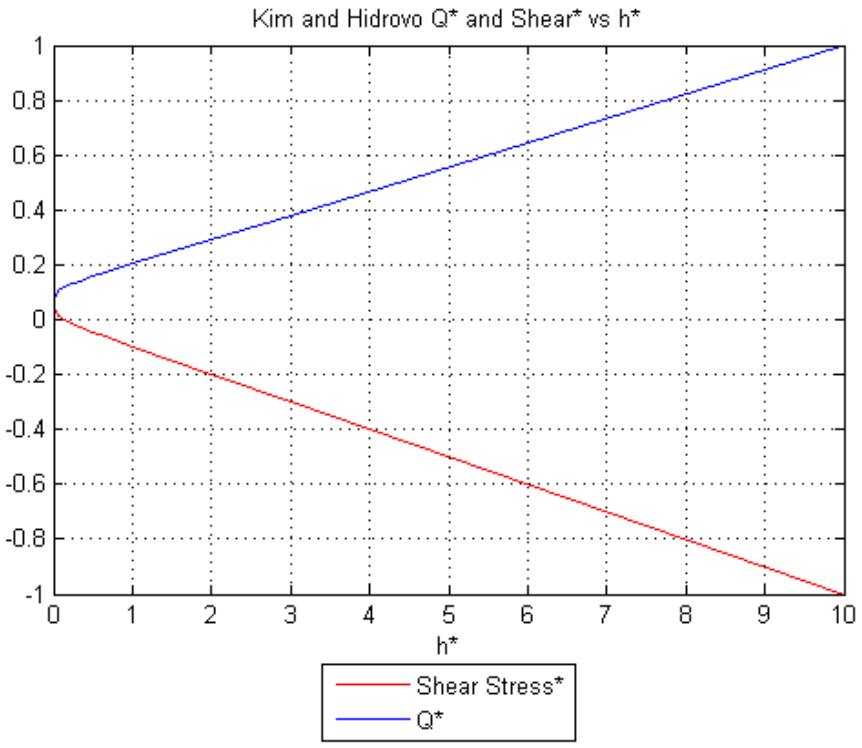

Figure 3.8: Combined and normalized shear stress* and Q* plot

Figure 3.9 shows a zoomed in version of figure 3.8 and reinforces the shear-stress and Couette-Poiseuille balance. At the critical h* value of approximately 0.12, the shear stress changes signs and hence the Q* transitions to a linear regime.

Modeling in COMSOL also confirms the velocity profile shift that occurs at the critical h*. Figure 3.10 shows a COMSOL velocity surface plot of a channel of water flowing on-top of a very thin channel of air, representative of a low h* case. Colors are used to indicate velocity magnitudes--higher velocities with red, orange and yellow while lower velocities are painted with green, light blue and dark blue. In figure 3.10 the normalized velocity profiles are shown--the red line indicates the

location of the interface and it is important to note that at the low h* case the water's velocity profile has a negative slope.

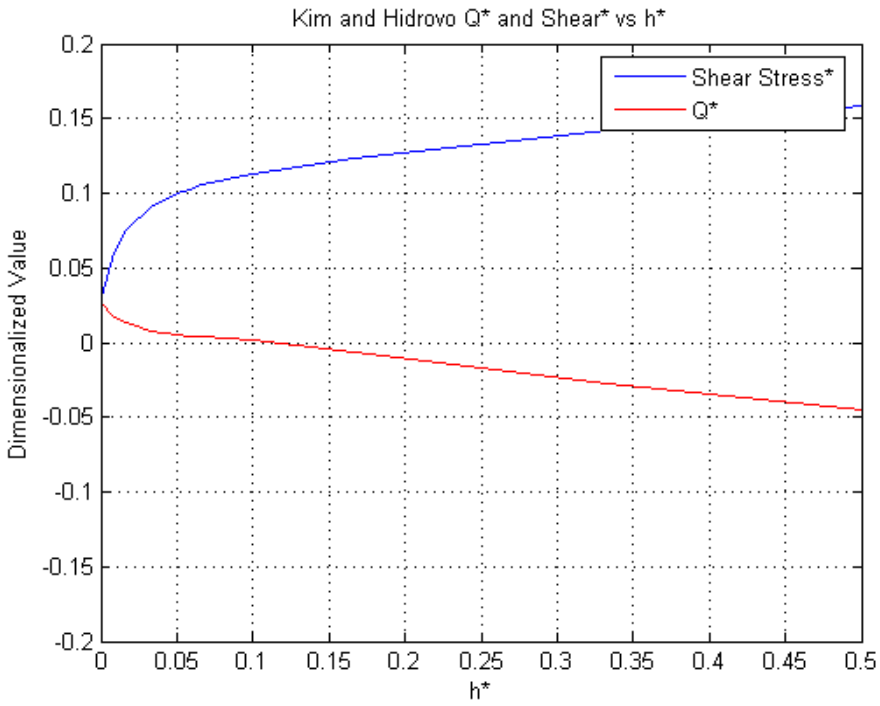

Figure 3.9: Zoomed in Shear plot

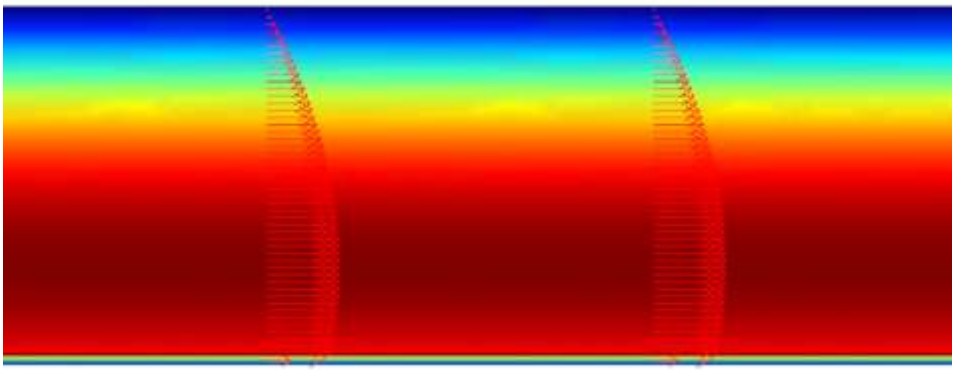

Figure 3.10: Combined and normalized shear stress* and Q* plot

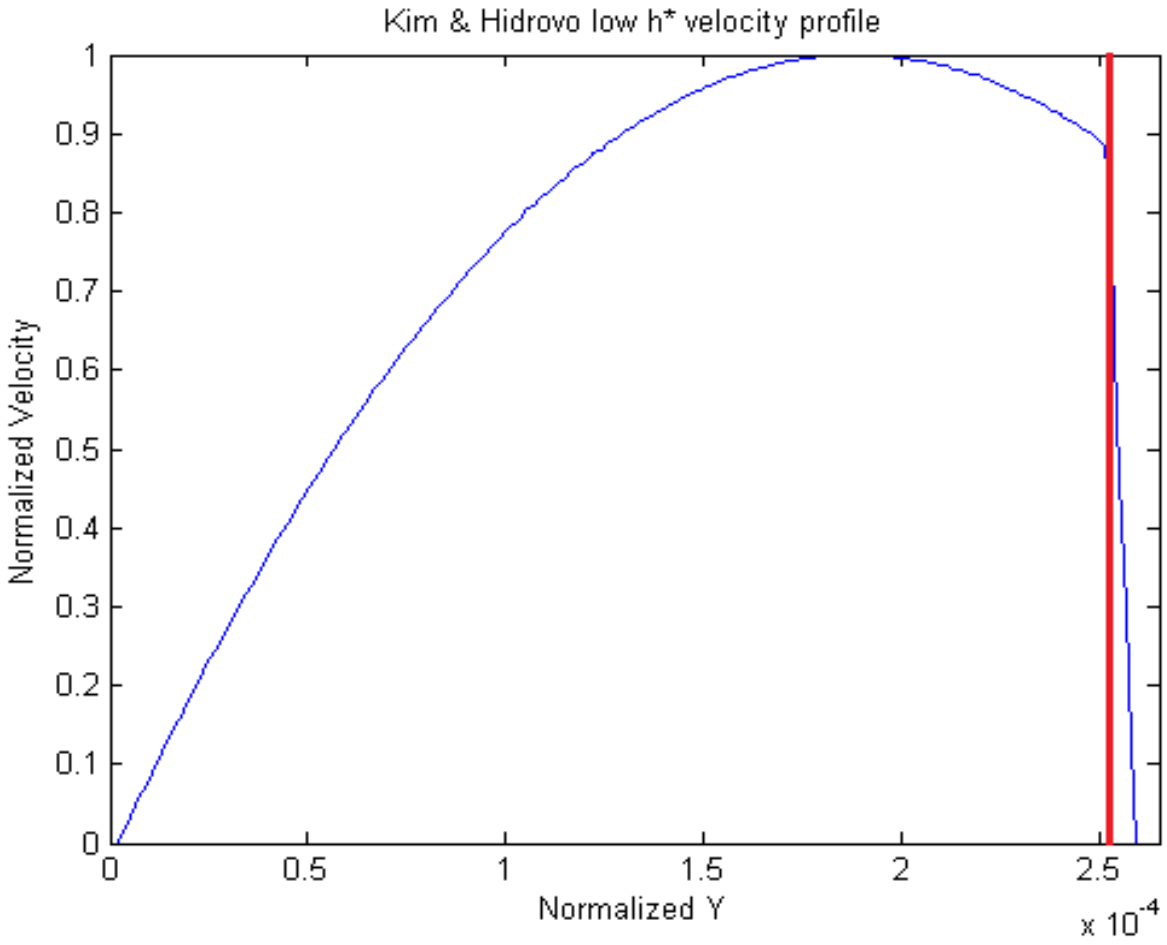

Figure 3.11: Velocity profile for low h* case with red line denoting interface

In the large h* case modeled in figures 3.12 the air channel is much larger than the water channel and hence the air flow will dominate the microchannel flow regime. However this times the water velocity at the interface has a positive slope and hence it switching signs, leading to the 2nd flow regime.

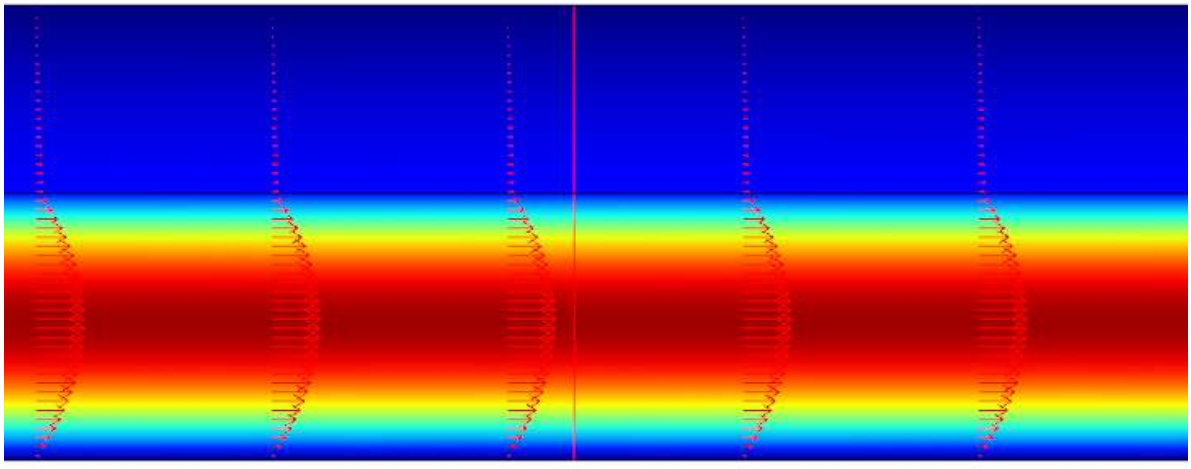

Figure 3.12: COMSOL high h* case

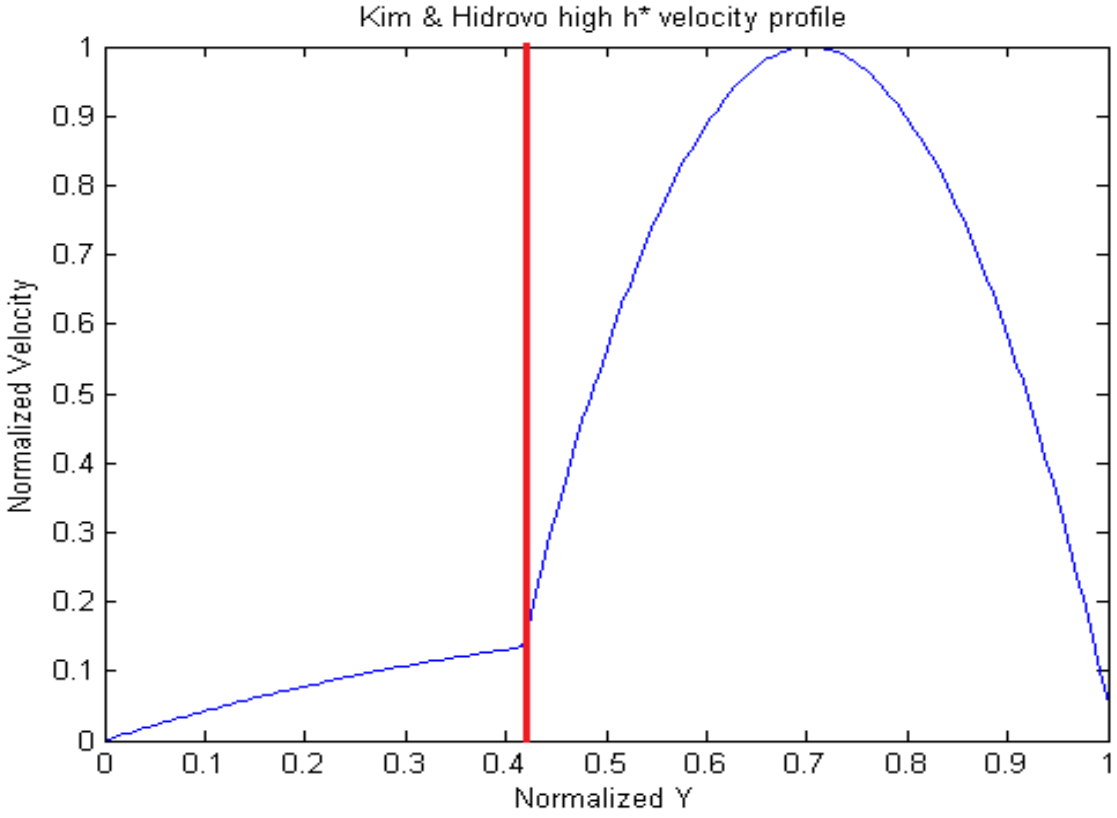

Figure 3.13: Velocity profile for high h* case with red line denoting interface

In summary, the Kim & Hidrovo derivation utilizes a two-phase fluid system with a common pressure gradient and absence of surface roughness features. It predicts a two regime system in which first the water flow is driven by a Poiseuille condition and then transitions to an air-flow driven Couette case, ultimately resulting in a unbounded Q* and frictional reduction.

3.4 ENRIGHT DERIVATION

The previous derivation presents an idealized case of water and air slip under a common pressure gradient. However under the presence of an air layer bounding Cassie-Baxter texturing state, the water and air flows are not typically subject to the same pressure gradients. Enright developed an analytical model that takes into account the existence of two different pressure gradients acting upon the water and air layers. Enright also included the assumption that surface roughness elements were present but their separation distances were extremely large, relative to the cavity heights. While this assumption isn't valid in realistic microchannels where the separation distance is on order of the microchannel width, it still provides an idealized benchmark. Enright assumed a planar water-air interface and that the largely separated surface elements induced a recirculating trapped air-layer with no-net flow[24] .

The Enright model follows the geometry depicted in figure 3.14 and is very similar to the previous geometry (Figure 3.1) except for a differing nomenclature and coordinate system. However, the key non-dimensional parameters will be defined the same for continuity between the two models.

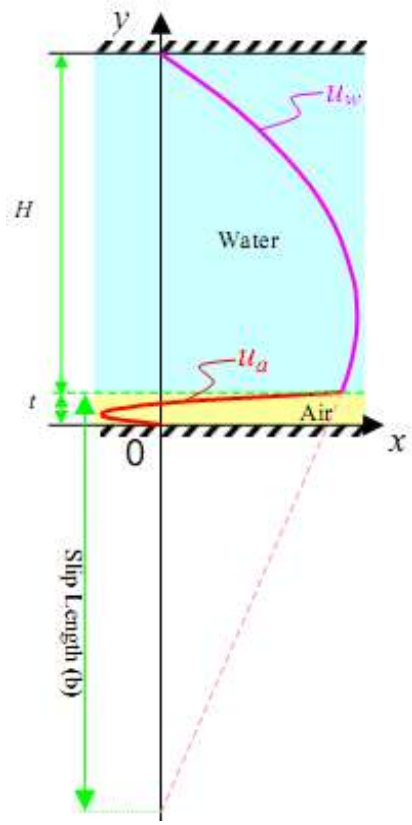

Figure 3.14: Enright air-layer model

Similar to equation (0.8) a coupled system of Navier-Stokes equations for the water and air streams are introduced.

$$\frac{d^2 u_{water}}{dy^2} = \frac{1}{\mu_{water}} \left(\frac{dp_{water}}{dx} \right) \tag{0.41}$$

$$\frac{d^2 u_{air}}{dy^2} = \frac{1}{\mu_{air}} \left(\frac{dp_{air}}{dx} \right) \tag{0.42}$$

The following no-slip, slip and interfacial boundary conditions are employed and are identical to boundary conditions applied from the previous section.

$$
\begin{aligned}
&u_{water} = 0 \ @ \ y = h_w + h_{air} \\
&u_{air} = 0 \ @ \ y = 0 \\
&u_{air} = u_{water} @ \ y = h_{air} \\
&\mu_{air} \frac{du_{air}}{dy} = \mu_{water} \frac{du_{water}}{dy} \ @ \ y = h_{air}
\end{aligned}
\tag{0.43}
$$

However due to the presence of two differing pressure gradients the inclusion of a recirculation boundary condition is essential. The following condition constrains the trapped air-layer with no net flow.

$$
\int_0^{h_{air}} u_{air} dy = 0 \tag{0.44}
$$

Applying boundary conditions (0.43) and (0.44) to (0.41) and (0.42) allows the subsequent integration constants to be solved and hence the air and water velocities can be expressed as a function of the water pressure gradient. The resultant water and air velocity profiles are the following.

$$
u_w = \left(\frac{dp}{dx}\right) \frac{\left(h_{air} - h_{water} + y\right)}{2\mu_w \left(-h_{air}\mu_w + 8h_{air}\mu_a - 4h_{water}\mu_a\right)} * \left(-3{h_{air}}^2 + 8{h_{air}}^2\mu_a + h_{air}\mu_a y + h_{water}h_{air}u_w - 4h_{water}h_{air}\mu_a - 8h_{air}\mu_a y \right.
\tag{0.45}
$$

$$
u_a = \left(\frac{dp}{dx}\right) \frac{\left(-h_{water} + 2h_{air}\right)^2 \left(-3y + 2h_{air}\right) y}{2h_{air} \left(-h_{air}\mu_w + 8h_{air}\mu_a - 4h_{water}\mu_a\right)} \tag{0.46}
$$

Allow y to be equal to the interface height, h_{air}, gives a slip velocity as follows:

$$u_{slip} = \left(\frac{dp}{dx}\right)\frac{-(2h_{air}-3)(2h_{air}-h_{water})^2}{((\mu_a - 8\mu_w)h_{air} + 4\mu_a h_{water})} \qquad (0.47)$$

Enright plotted his results in terms of fRe or Poiseuille number and noted that at sufficiently large values of h_{air} /H, or h*, fRe reached an asymptotic value, as seen in the previously reproduced figure 1.6.

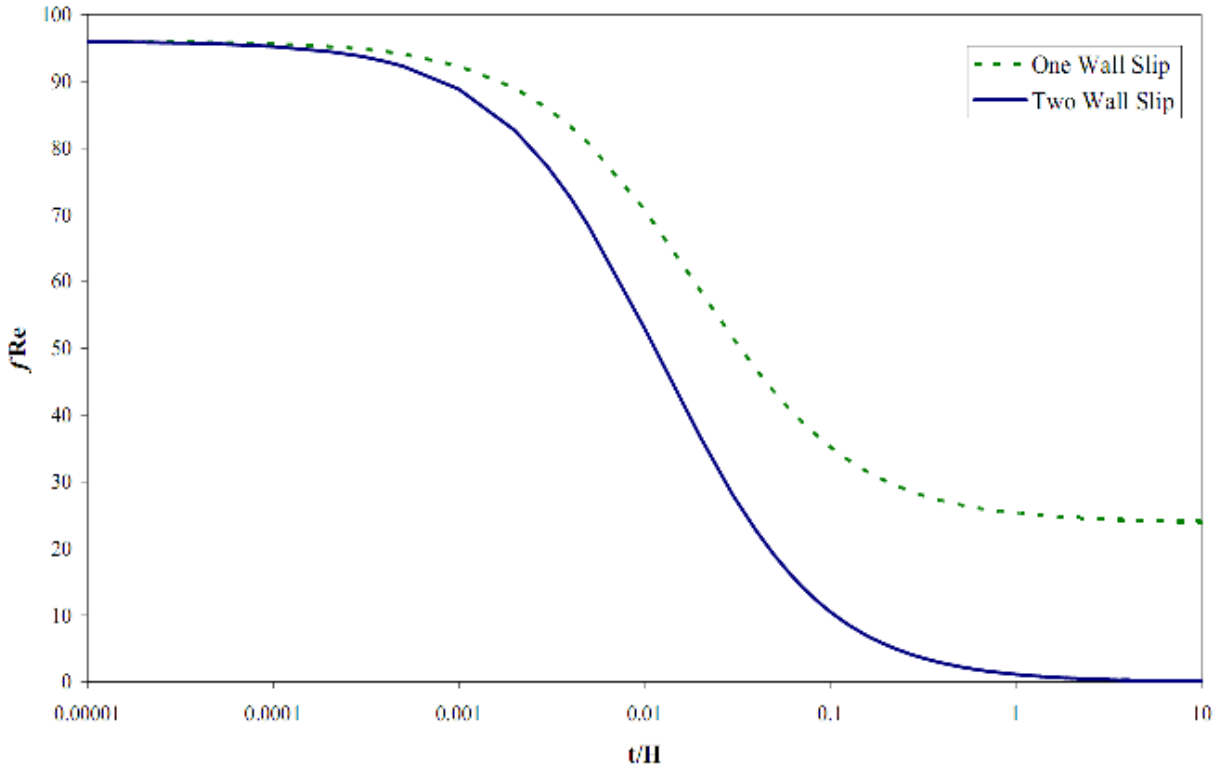

Figure 1.3: Enright model showing asymptotic behavior of flow rate [24]

Enright noted this asymptotic limit but did not go into further detail about its origins. Following the previous analysis for the Kim & Hidrovo model, a U* vs h* and a Q*

vs h* plot can be computed for the Enright model, as shown in figure 3.15 and figure 3.16.

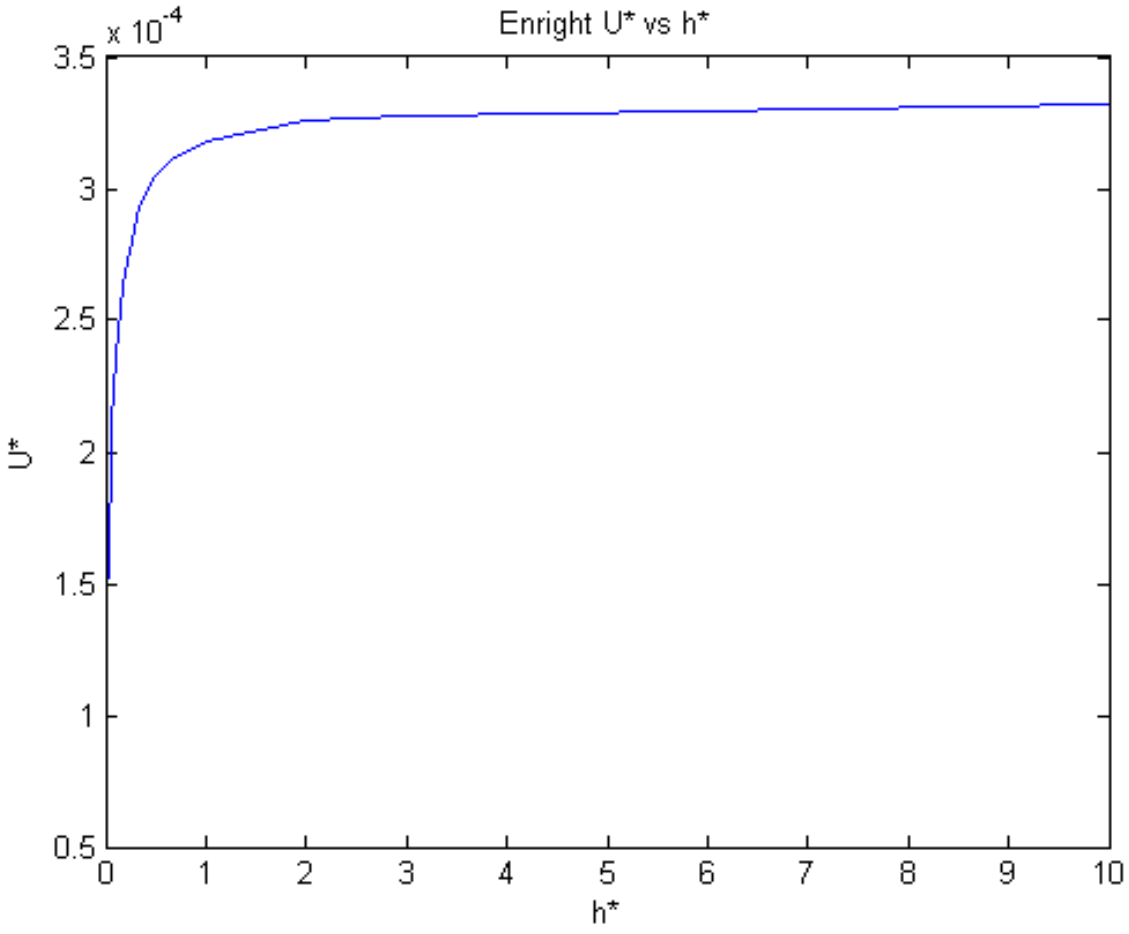

Figure 3.15: Enright U* vs h*

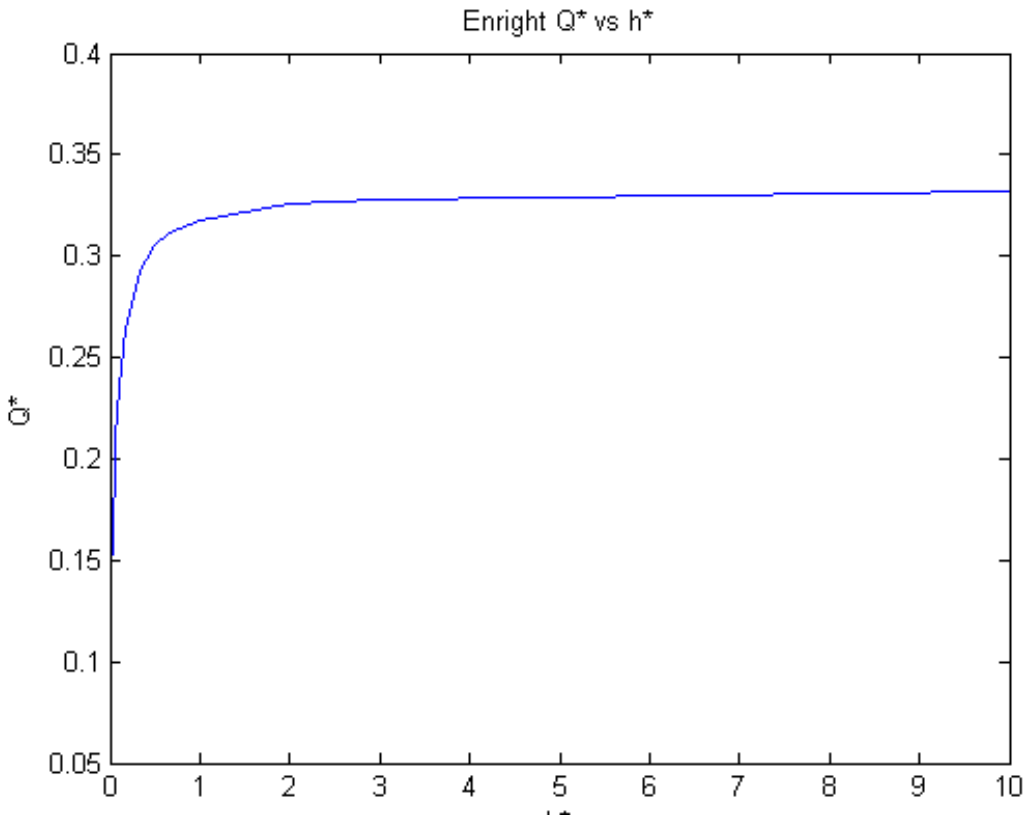

Figure 3.16: Enright Q* vs h*

Once again the U* and Q* plots have the same general shape and concavity--the flow -rate is dependent on the interfacial slip velocity and hence they should have similar properties. While the Enright Q* plot has the same rapid Q* increase at low h*'s, similar to the Kim & Hidrovo model, one drastic difference is the existence of a plateau effect at a critical h*. The Enright model predicts that as the air-layer or h* increases, there is only a slight increase in Q* and hence it appears to approach an asymptotic value.

This deviation from the Kim& Hidrovo derivation is due to the lack of a common pressure gradient and the recirculation constraint (0.44) for the air-layer. In this case the air-layer still acts as a reduced shear boundary for the water layer, due to the large difference in viscosities. However while the air-layer has an interfacial velocity provided by the water, the recirculation constraint causes the air-layer to be essentially stagnant. In the previous derivation, as the air-layer thickness grew, there was a transition to a Couette dominated flow due to the common pressure gradient accelerating the air-layer. This resulted in the air-layer dominating the flow-profile and essentially dragging the water-layer with it and hence allowing for higher flow-rate and Q*. In the Enright case the air-layer does not have a common pressure gradient and recirculates, and thus there is no transition to the Couette dominated flow which resulted in an unbridled flow-rate.

At first the water-layer will exhibit the same Poiseuille dominated flow at low h* associated with a small air-layer--the air-layer will provide a shear-free layer which gives rise to the slip condition. However as the air-layer grows, the recirculation constraint causes the back-flow in the cavity to increase as well. Ultimately the water-layer will plateau since it'll reach a critical h* in which the air-layer retard's its development.

Figure 3.18 depicts the velocity magnitude through the microchannel with the red line denoting the interface. Since the plot shows the velocity magnitude and hence absolute value, the small hump at the bottom of the channel represents the recirculation in the air-layer. At low h* vases the Enright velocity plot has a negative slope similar to the Kim & Hidrovo derivation, indicating Pouselle dominated flow.

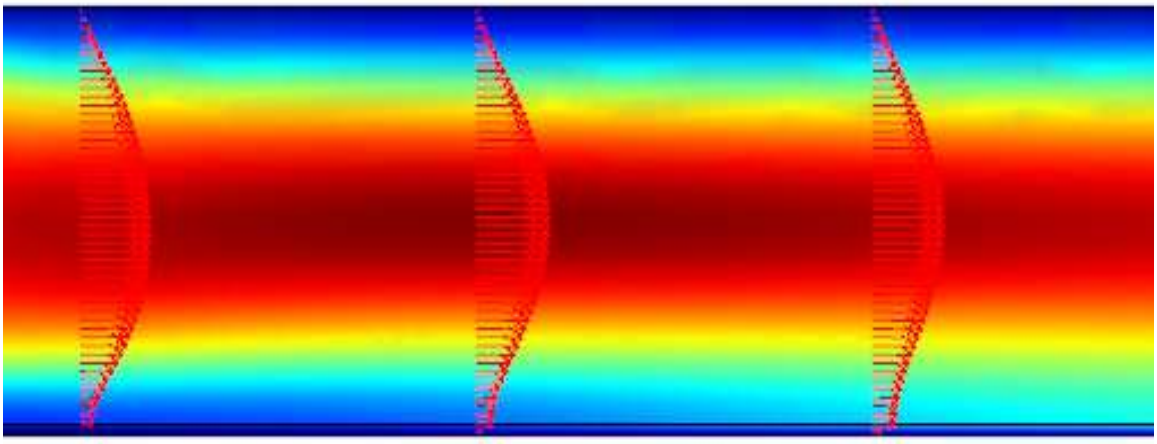

Figure 3.17: COMSOL model of low h* Enright case

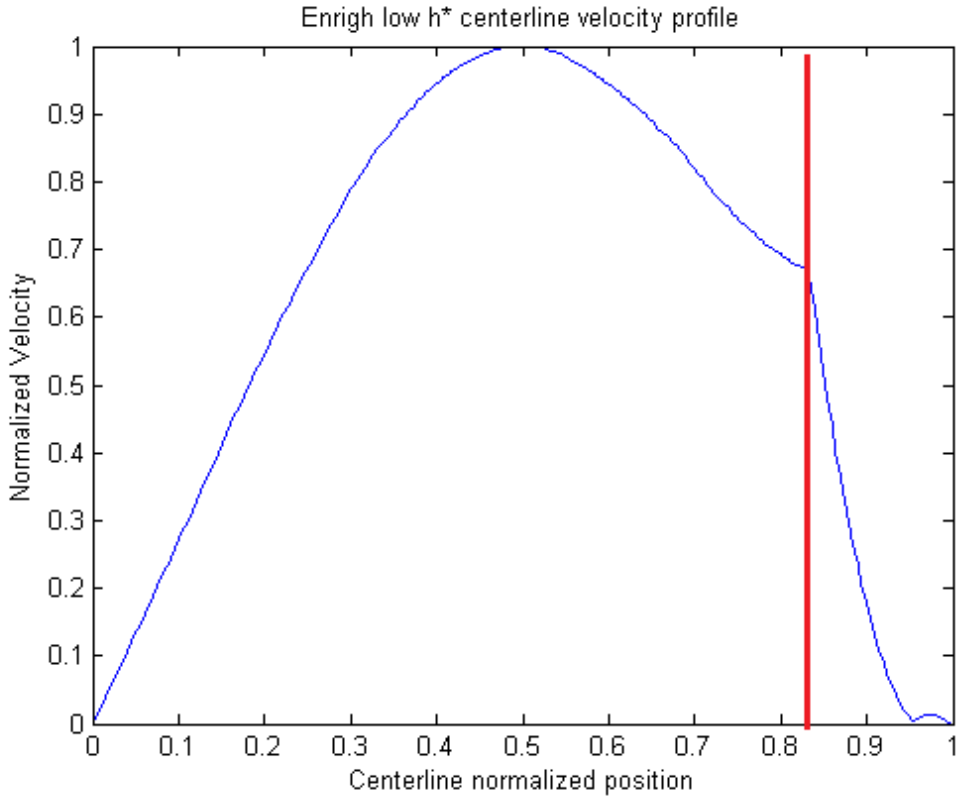

Figure 3.18: Enright low h* centerline velocity profile with red interface line

However at high h* values, as seen in figure 3.19 and 3.20, the velocity keeps the negative slope and does not change signs and there is no transition to the Couette dominated flow. As the air-layer grows, there is a critical thickness in which the shear-free boundary layer provides enhanced flow for the water-layer and beyond that the recirculation constraint then works against it. As the water layer develops the air-layer recirculation magnitude grows, as seen by the higher velocity in the hump in figure 3.19 and hence the water-flow is retarded and plateaus.

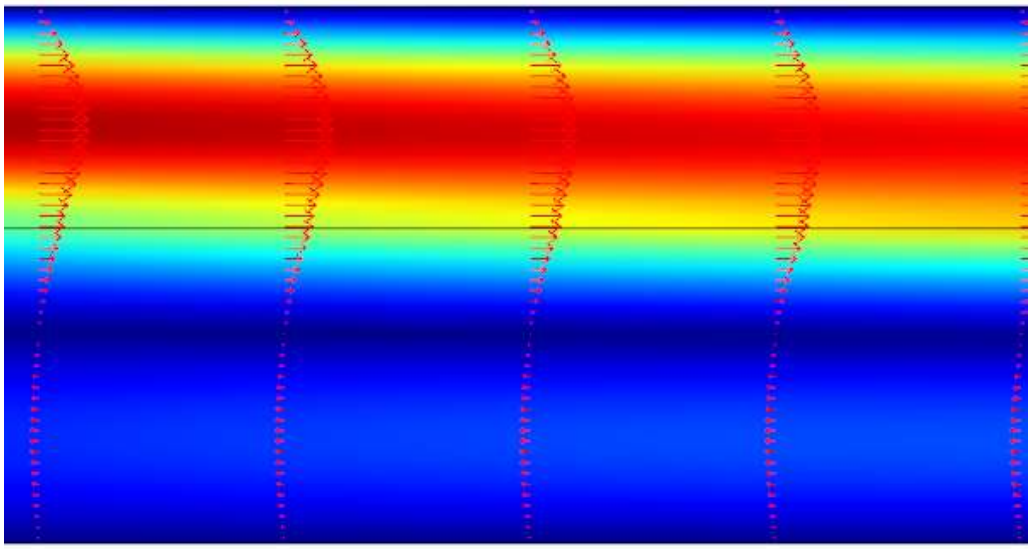

Figure 3.19: Enright COMSOL high h* case

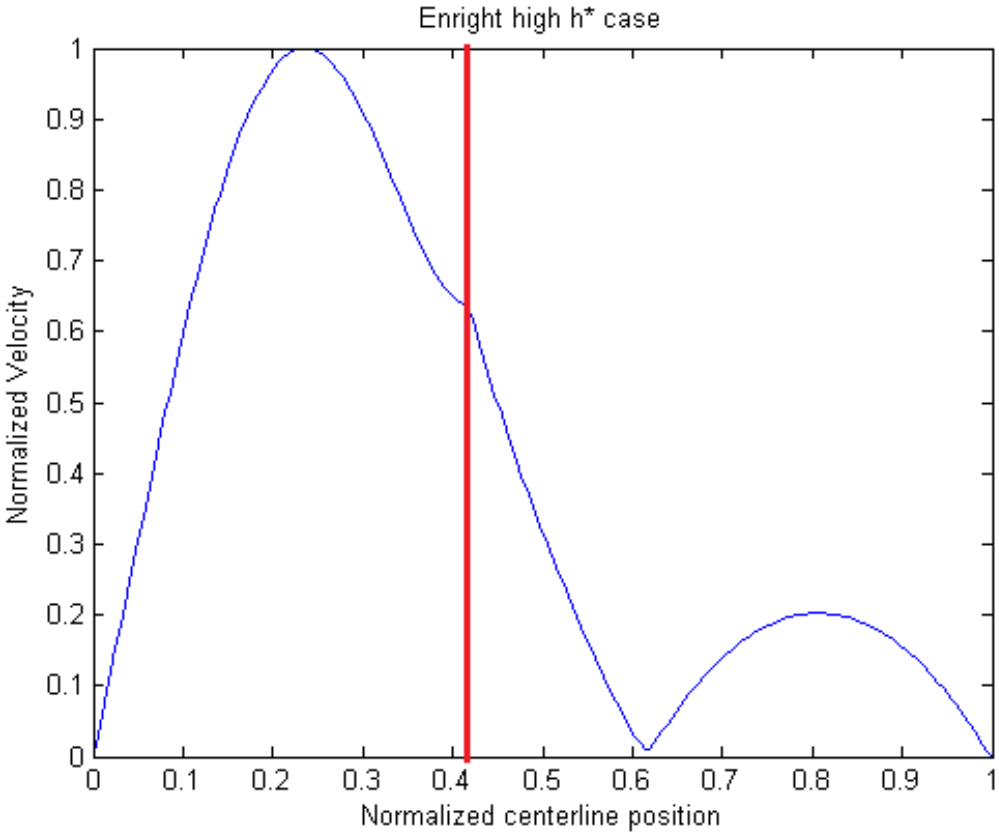

Figure 3.20: Enright high h* centerline velocity profile with red interface line

It is now apparent that the constraint on the air cavity limits the flow development and causes an asymptotic value. The next chapter will ultimately show that the effect Enright predicted is due to recirculation.

3.5 ANALYTICAL MODEL COMPARISON

Both the Kim & Hidrovo model and Enright model can be compared against each other in order to evaluate their ability to flow water and hence frictional reduction.

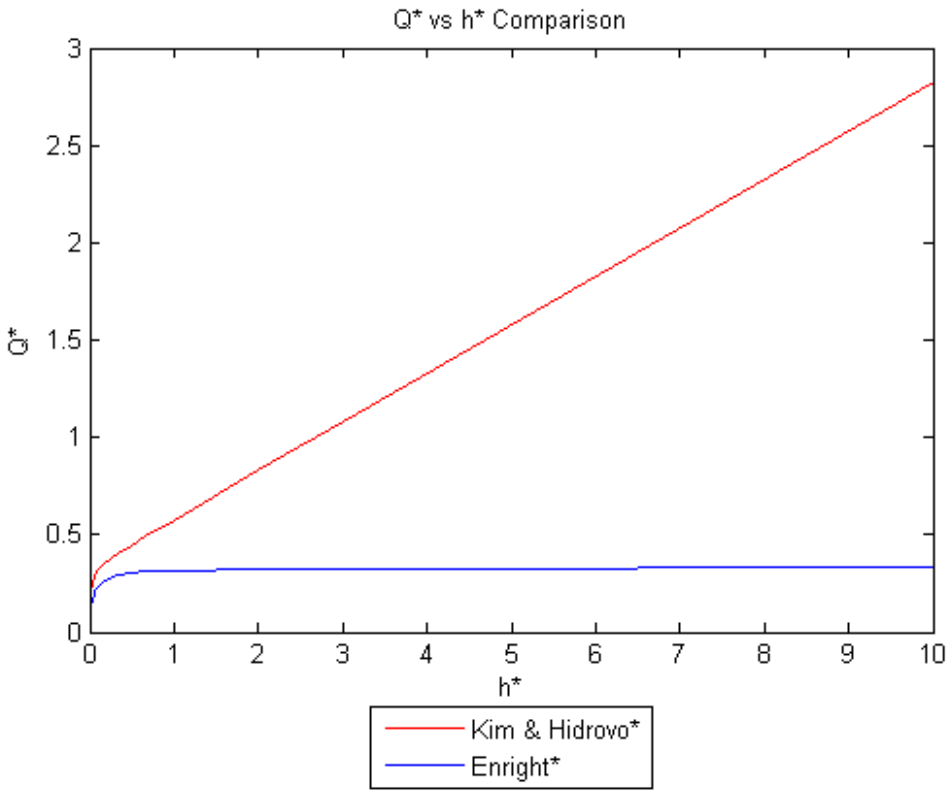

Figure 3.21: Comparison of models

Figure 3.21 shows a comparison of both models based on their Q*s. In terms of trends, the Kim & Hidrovo model predicts a higher Q* and hence water flow rate as a function of h*. As discussed previously, this higher Q* is a result of a common pressure gradient on both the water and air flows that causes an unbounded slip velocity which ultimately yields to an unbounded Q*.

The Enright model incorporates differing pressure gradients for the water and air flow as well as recirculation--a more realistic constraint. As discussed before, the Enright Q* plateaus due to the recirculation constraint which prevents an unbounded slip velocity and hence a bounded Q*. More importantly the Enright Q* is a much lower than the Kim & Hidrovo model, indicating that the recirculation in microchannels inherently causes a decreases in performance.

Relying on the previous relation from (0.36), figure 3.21 can be expressed instead in terms of the Poisuelle number or fRe.

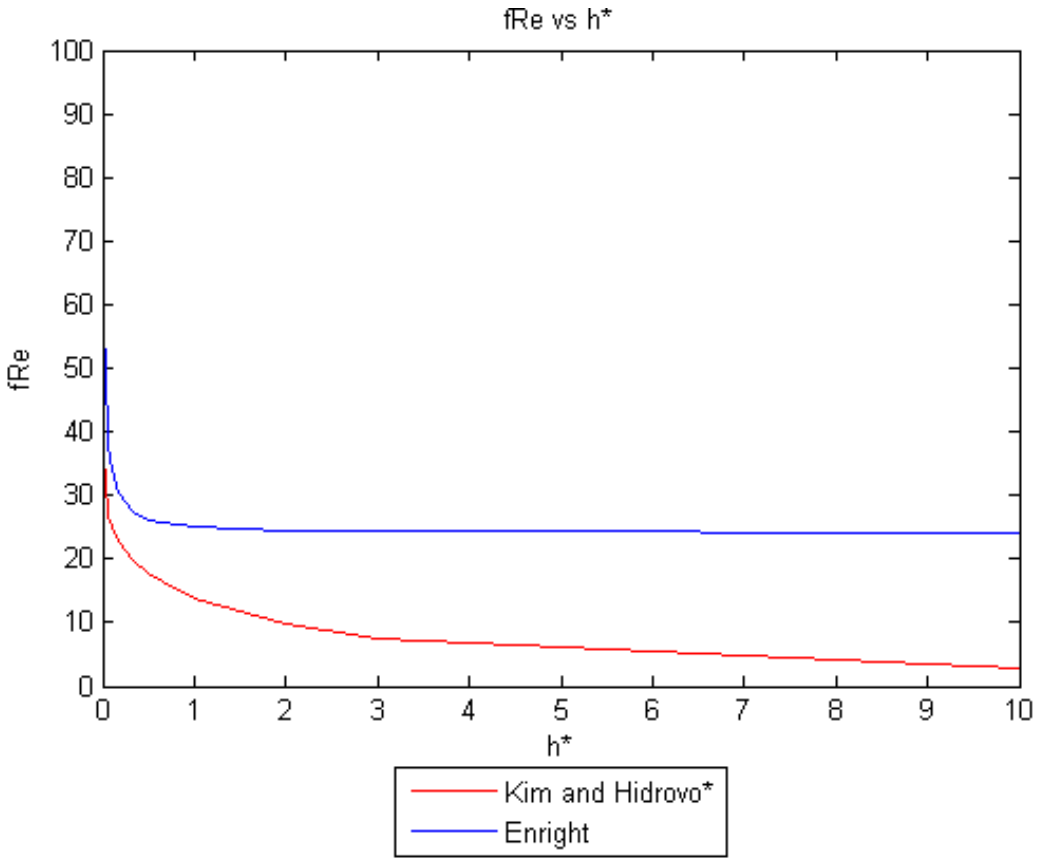

Figure 3.21: Comparison of models

At low h* values both models converge at a Poisuelle number of 96, the expected value for fully developed flow within a square duct. However as the air layer or h* increases, the fRe for the Kim & Hidrovo model decrease proportionally due to the unbounded slip-length providing frictional reduction.

The Enright model instead converges to a fRe value of approximately 24 or 1/4 of the original value, due to the no-net air flow providing a limit to the water flow rate. The Enright model is useful since it too represents another idealized step in the fluid dynamics of microchannels--it provides a theoretical ceiling on microchannel performance and flow rate. However, Enright did not provide an explanation for this plateauing effect. Furthermore this model is based on the extreme case in which there is a very large separation between the surface roughness elements. In laboratory settings this isn't a realistic assumption since fabrication techniques can limit the cavity distances and most microchannels have cavity lengths on order of the microchannel width. Finally, Joshi's simulations concluded that as the cavity length increases, the Cassie-Baxter state can collapse and cause Wenzel penetration. These results in the air-layer escaping the cavity and the frictional reduction benefits of the air's shear free layer are lost. Hence the assumption of a very wide cavity in which the end-wall effects are neglected is not realistic.

Chapter 4: Computational Model and Results

4.1 Computational Model Introduction

The Kim & Hidrovo derivation addressed multiphase flow under a common pressure gradient while the Enright derivation identified a plateauing effect with the introduction of idealized microtexturing. However in the research setting, microchannels have air pockets that are between finite surface roughness elements. There have not been any models or studies that analyzed the combined effect of recirculation, repeated cavities and wall effects. Furthermore, the plateauing of the flow-rate or Q* is not completely understood. The comprehension of these combined effects in realistic microchannels is the primary motivation behind this computational study.

4.2 Computational Methodology and Assumptions

The author used COMSOL Multiphysics version 3.5a with the MEMS module for increased functionality with microfluidic applications. Geometries were designed exclusively within the software's in-house CAD developer and thermal-fluid properties were assumed constant for simplicity. Post processing data analysis was employed within the COMSOL workspace though minor data manipulation and graphing was performed in Microsoft Excel or MATLAB.

The first major overriding assumption was that the microchannel was of closed geometry and hence had cavities along the pressurized water flow—as seen in figure 4.1. The author also assumed that the microchannels exhibited a *perfect* Cassie-Baxter state, implying that the air cavities were completely filled with air and thus the water was confined to a fixed channel height. Most importantly in assuming a perfect Cassie-Baxter state, the air-water interfaces were steady-state, planar and stationary. It is important to note that the fluid domains, the channel and cavities, are fixed and therefore mixing of the two fluids does not occur. While experimental evidence has shown an asymmetrical water penetration within the cavity over time, a fixed water-air interface would still suffice for initial flow rates where the water-air interface typically remains intact. The ramifications of these assumptions not only allow simpler simulations but signify that the results would reflect an ideal microchannel operation and hence could serve as a benchmark and investigative tool to analyze the geometry impact on frictional reduction.

4.3 MODEL GEOMETRY, BOUNDARY CONDITIONS AND MESH

The microchannel consists of a series of repeated air-filled cavities below a stream of pressurized water, as depicted in figure 4.1. Unlike previous analytical models [23, 24], the air is not pressurized and therefore the only forces acting upon the air-layer will be generated by the water stream.

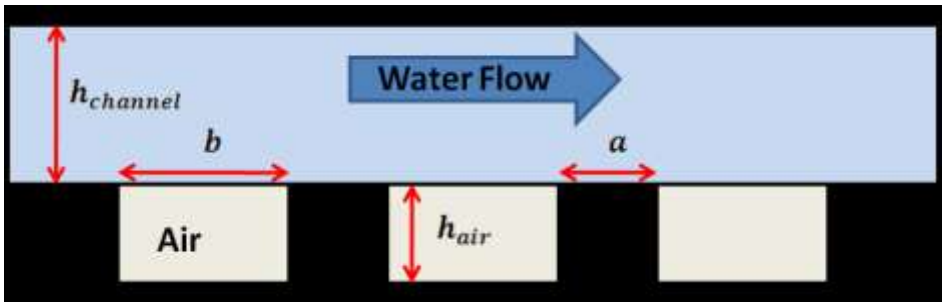

Figure 4.1: COMSOL Flow geometry

The microchannel length and channel height were fixed to mimic experimental conditions and provide simplicity. Table 4.1 summarizes the key parameters used in the simulation.

Table 4-1: COMSOL Parameters

$h_{water} = 60$ microns	$\mu_{air} = 1.79\text{E-}5$ Pa-s	$P_{inlet} = [0 - 3000$ Pa$]$
$h_{air} = [0$ - 600 microns$]$	$\mu_{water} = 1.12\text{E-}3$ Pa-s	$P_{outlet} = 0$ Pa

The goal of the simulations is to investigate frictional reduction in microchannels and hence the slip-boundary condition is pivotal in maintaining realism with experimental microchannels. The water-air interface was modeled by applying weak-boundary constraints to exclude transverse velocities and therefore allowing an interfacial slip velocity. All other surfaces were constrained with a no-slip condition. In order to properly simulate testing procedures, the inlet water-stream

of the microchannel was exposed to varying pressure gradients from 250 Pascals to 3000 Pascal, and the outlet was defined at 0 Pascals.

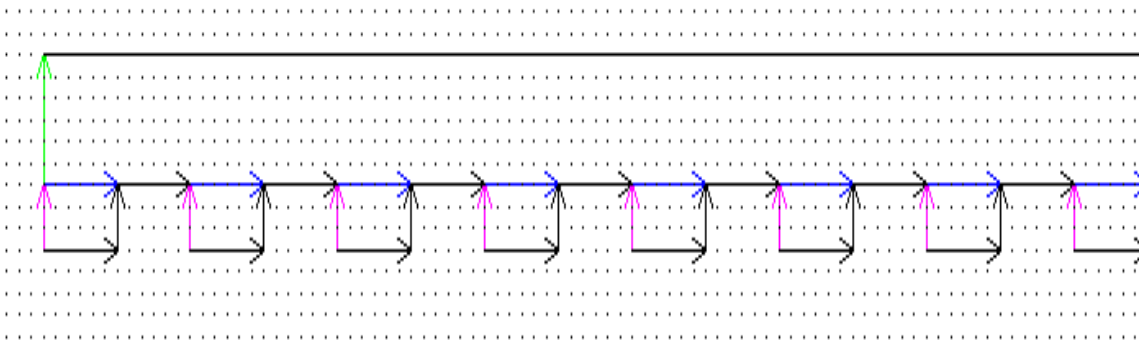

Figure 4.2: CAD Geometric representation of microchannel

An advancing triangle-front mesh was used that was auto-optimized by COMSOL with each refinement. While other meshes were available and there is a wealth of literature on the best mesh generations, the author chose the same meshing methodology in order to remain consistent and to eliminate numerical errors arising from conflicting mesh patterns. Grid independence was achieved through extra-fine mesh refinement with a minimum of 100,000 elements.

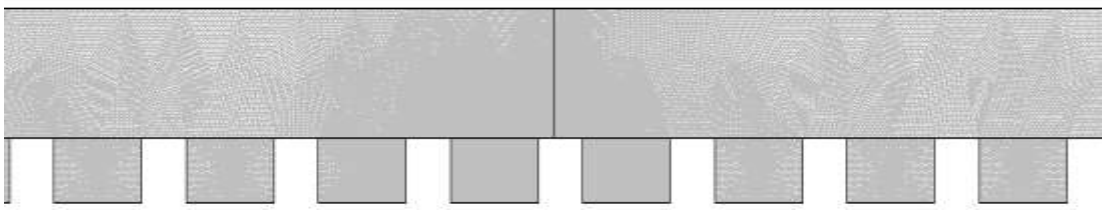

Figure 4.3: Extra fine mesh with advancing triangle front to ensure grid independence

4.4 POST PROCESSING AND VISUALIZATION

Post processing was necessary to calculate the necessary flow parameters such as velocity, shear stress or pressure gradients. COMSOL's internal post-processing module was used to stream line the process. Gradients were obtained by boundary integration along the plane of interest and relevant terms were calculated by algebraic manipulation of the integration values with their corresponding planar dimensions. Furthermore, data-sets were imported into Excel where more complex functions such as friction factor or slip length were calculated and plotted. In terms of visualization, COMSOL's standard color palette and arrow plots were utilized.

Arrow plots were adjusted accordingly for proper resolution and clarity of images. Figure 4.4 shows an example velocity surface plot of the microchannel using a standard rainbow palette. Velocity magnitudes are expressed as colors in the following descending order: red, orange, yellow, cyan and dark blue. Once again, the water-air interface is fixed and stationary, therefore figure 4.4 depicts the velocity magnitudes for the water and air domains, which do not mix.

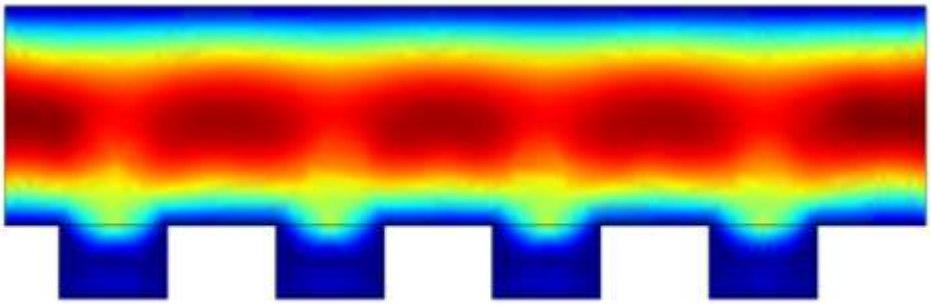

Figure 4.4: Example COMSOL velocity field visualization with standard color palette

4.5 FLOW RATE AS A FUNCTION OF H*

Following the previously defined non-dimensional parameters, a Q* vs h* plot was calculated based on multiple COMSOL runs and depicted in figure 4.5. There are two main observations that can seen from figure 4.5; first there is a plateauing effect, similar to Enright, indicating a terminal flow-rate. This is in fact comforting since this COMSOL model is based on an advanced Enright case and hence it is expected to have similar characteristics. Second, there is the existence of a pressure spread between the Q* values, as seen in figure 4.5

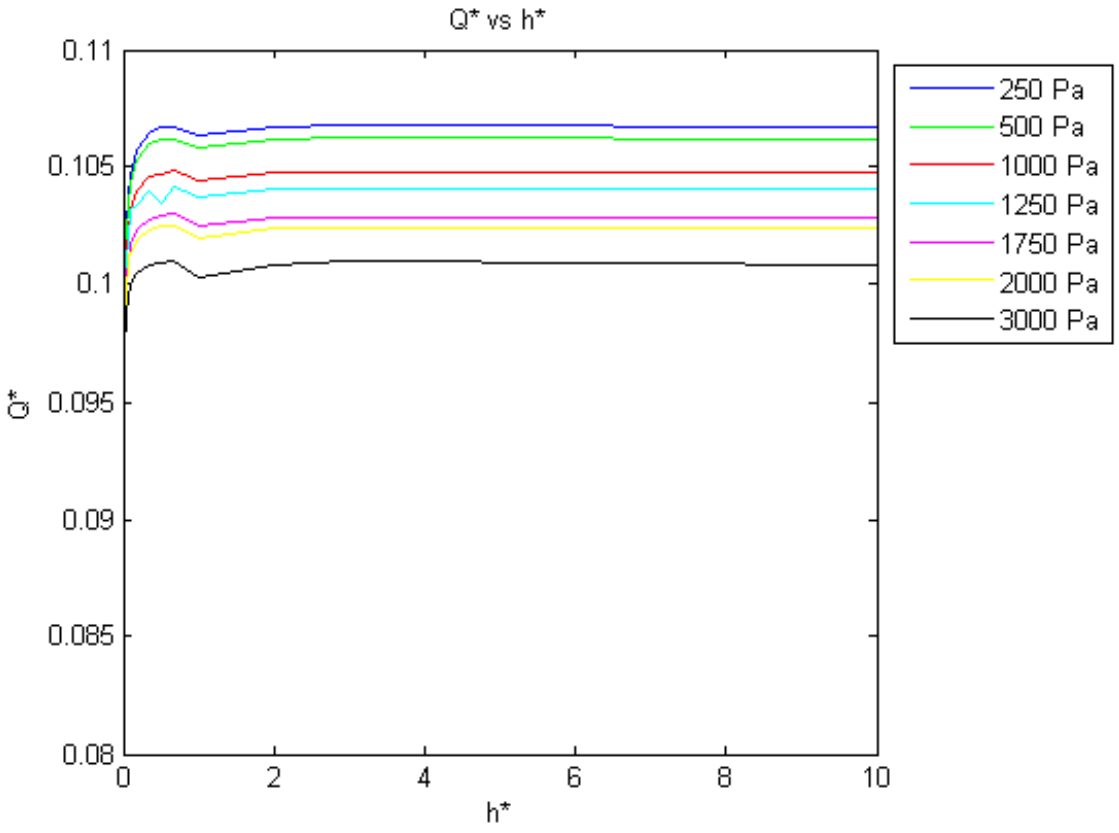

Figure 4.5: COMSOL Q* vs h*

4.6 PRESSURE AND DEVELOPING EFFECTS

It isn't intuitive that a spread exists between the Q* values, specifically since Q* was defined such that it was non-dimensional and hence finite dp/dx terms should cause the collapse on a single form. This spread effect is caused by the water developing region when entering the air cavities of the microchannel. The Enright model assumed that there is a large separation between the surface roughness features. However when the surface roughness separation decreases and is on order of magnitude of the microchannel dimensions, as in this COMSOL case, it is expected that developing effects will play a more prominent role. Due to the difference in magnitude of the water and air viscosities, the water profile is unable to become fully developed each time it enters an air cavity. To illustrate this point, normalized velocity profiles were taken before entry into the air cavity, within the air cavity and upon exiting the air cavity for various pressures--as depicted in figure 4.6.

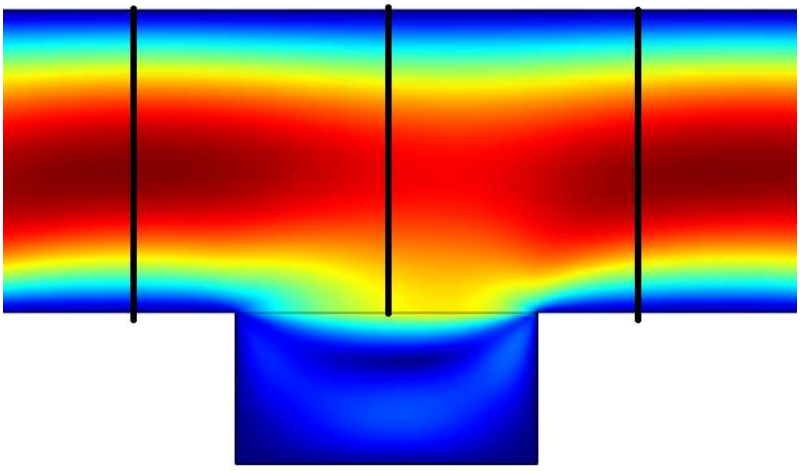

Figure 4.6: Positions for velocity measurements for entrance effect

Before entering the channel and when in contact with the wall, the water profile is the same regardless of the pressure conditions or h*. This indicates that the water profile is fully developed when in contact with the wall and once again becomes fully-developed after exiting the microchannel. The entrance length for laminar pipe flow is typically correlated by the following equation.

$$0.06\,\mathrm{Re} = \frac{x}{D} \tag{0.48}$$

Velocity results showed that the Reynolds number for the water flow ranged from 0 to 5, giving an approximate entrance length of 20 microns or about 1/3 of the microchannel wall span, which were in line with the COMSOL measurements.

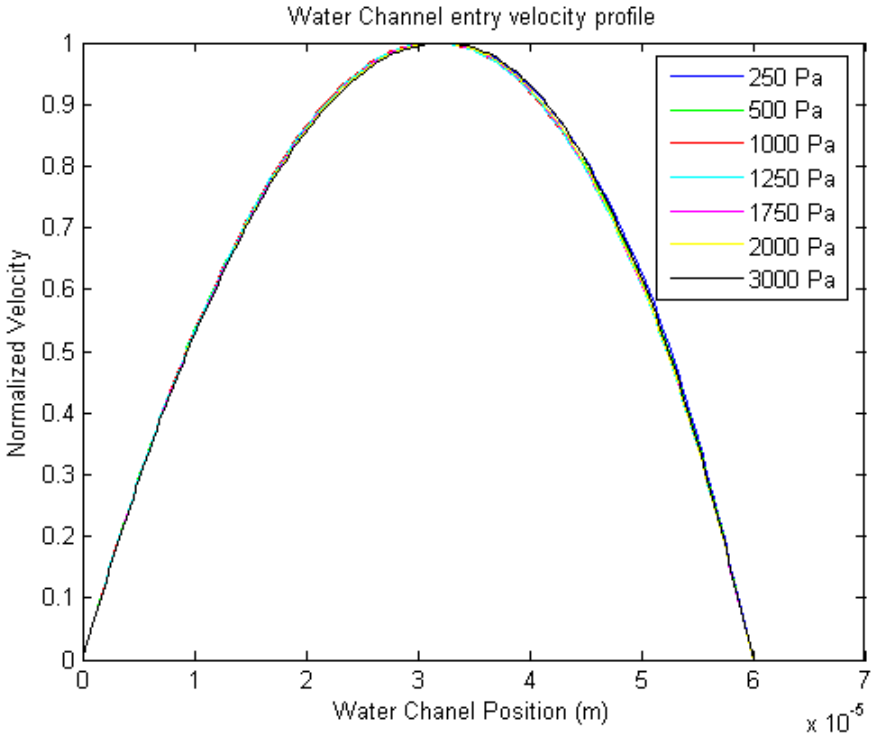

Figure 4.7: Velocity profiles before entering the air cavity

However when the water profile is within the channel, as depicted in figure 4.8, the velocity profiles do not collapse and a stratification occurs based on the pressure. This is observed throughout the gamut of h* values and within varying positions in the air-cavity. Hence, the air cavity and its slip layer amplify developing effects for the water flow and as a result the flow is not fully developed. The author varied the positions and lengths of the air cavity from 0.5 to 3 times the water channel width but found that the water profile did not collapse. Furthermore the use of (0.48) was not successful in predicting the entrance length for the shear-free air layer. This result highlights a key difference between this study and previous models; under finite surface element roughness separation, developing effects will play a larger role.

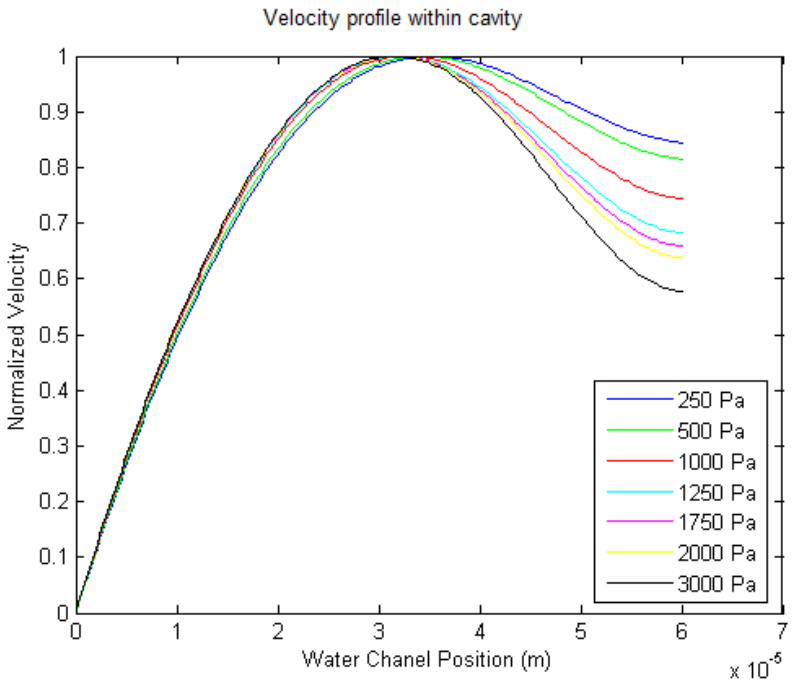

Figure 4.8: Velocity profiles within the air cavity

Just as the water exited the air cavity and made contact with the wall, the velocity profiles had slight deviations as depicted in figure 4.9. These discrepancies are a result of the entrance effects that distorted the velocity profile within the air channel. However, upon traveling approximately 20 micronson the "land" portion of the microchannel, the flow became fully-developed and velocity plots collapsed as similar to figure 4.7.

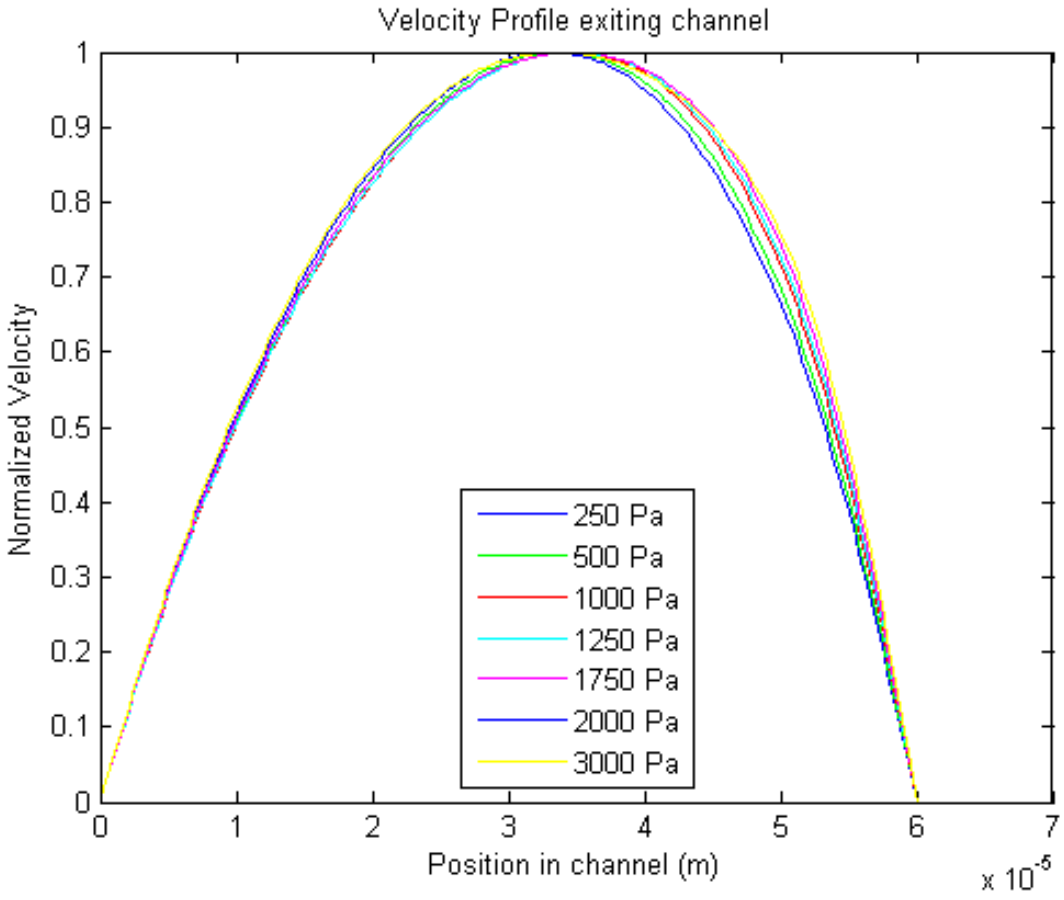

Figure 4.9: Velocity profiles after exiting the air cavity

Since the developing regions are a function of the applied pressure as well as the air cavity and hence properties of air, it is expected that changing the viscosity of air will amplify or dampen said entrance effects. It's expected that as the air approaches a no-slip or wall condition that the water profiles within the cavity will converge and become fully-developed. To illustrate this point the author varied the viscosity of air and then compared the spread between the lowest pressured Q* at 250 Pascals and the highest Q* at 3000 Pascals.

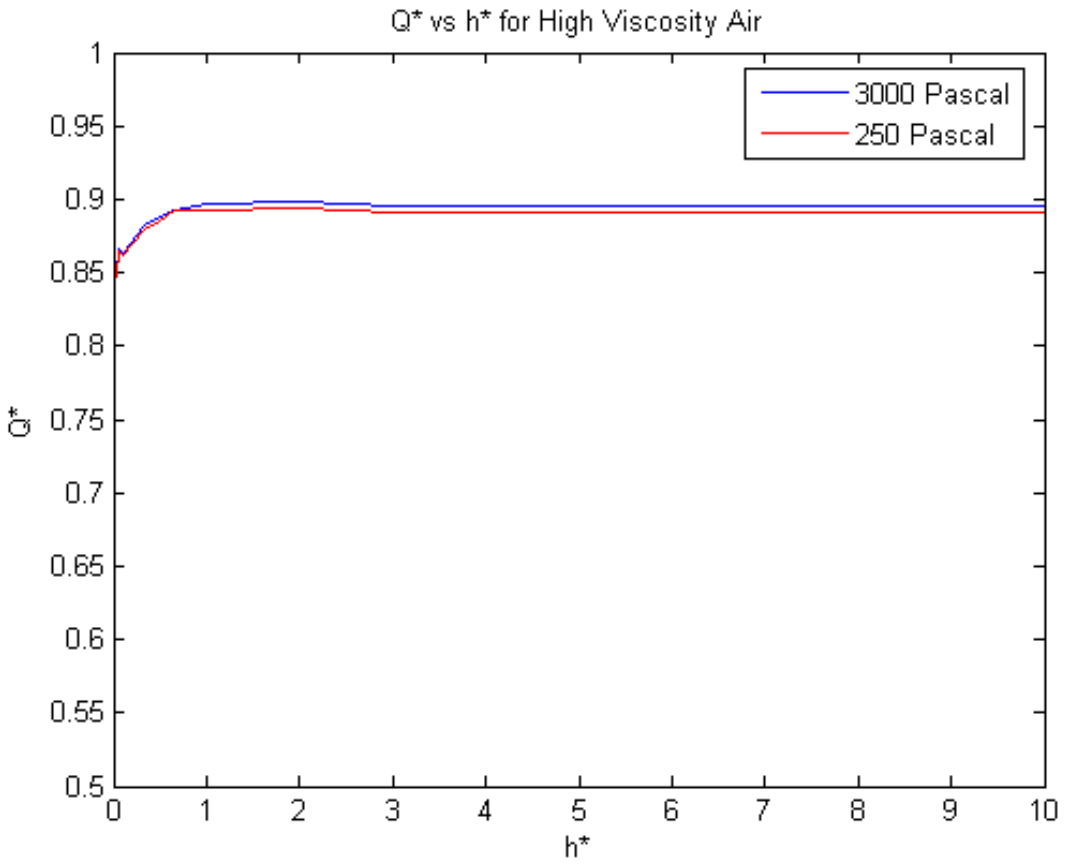

Figure 4.10: Viscous effects for Q*

When the viscosity of air was increased by 3 orders of magnitude, the shear free effect is dampened and hence the water flow will achieve full development. This manifests in the same Q* for a given pressure and is in contrast to the real case where developing effects will distort the Q* at a given pressure. The viscous Q*s are expected to be lower than the normal viscosity Q*s due to the reduction in slip effects as a result of the higher viscosity.

It is now apparent that the Q* spread seen in figure 4.5 is a result of entrance effects within the air-cavity--the velocity profiles are subjected to developing regions that vary depending on the applied pressure.

4.7 EFFECT OF RECIRCULATION

Visualization of stream lines and velocities give greater insight into the microchannel fluid dynamics compared to the previous analytical models. Specifically, the simulation highlights the existence of recirculation within the air-cavities, as seen in figure 4.11, which were not mentioned in the Enright model. The air cavity recirculation originates at the interface, where the water slip velocity drags the surrounding as it flows through the channel. The air velocity decays as the depth or distance from the interface increases, due to being farther away from the slip velocity. Due to the no-slip boundary condition at the wall and their small separation distance, there are y-velocity components that help promote x-velocity components in the opposite direction. The resultant is a clockwise recirculation flow within the air cavity that is reminiscent of the classical "lid driven cavity" problem [54].

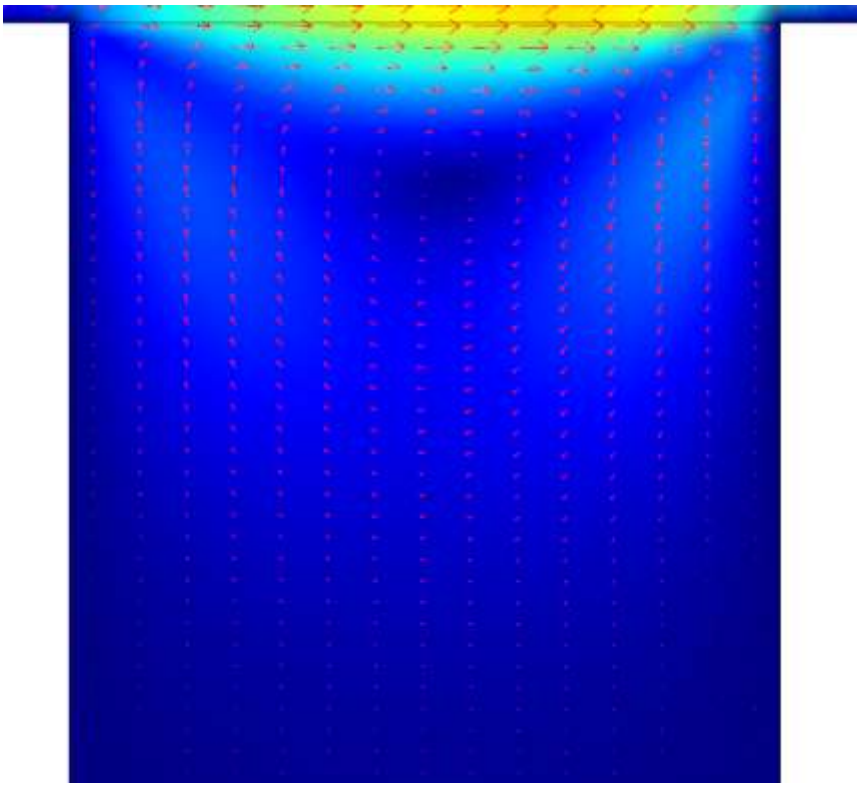

Figure 4.11: Air recirculation in microchannel

Figure 4.12 depicts the x-component, y-component and overall velocity magnitude longitudinally across the air-cavity of h*=1 (60 micron deep). The x-component is highest the interface, where it is equal to the slip-velocity and the y-velocity is zero due to the absence of transverse velocities across the interface.

The y-velocity component increases temporarily as the depth increases, due to recirculation at the walls. However both the x and y-components eventually decay as depth increases. The resultant eventually leads to a stagnation point as depicted in dark blue in figure 4.11. In addition a back flow is induced due to the closer proximity of the walls, which results in negative x and y velocity components. This

graphical and numerical visualization of the recirculation shows that the driving slip-velocity is also weakly constrained by an opposite velocity due to recirculation. As the pressure is increased and hence slip velocity increase, the opposing velocity should follow.

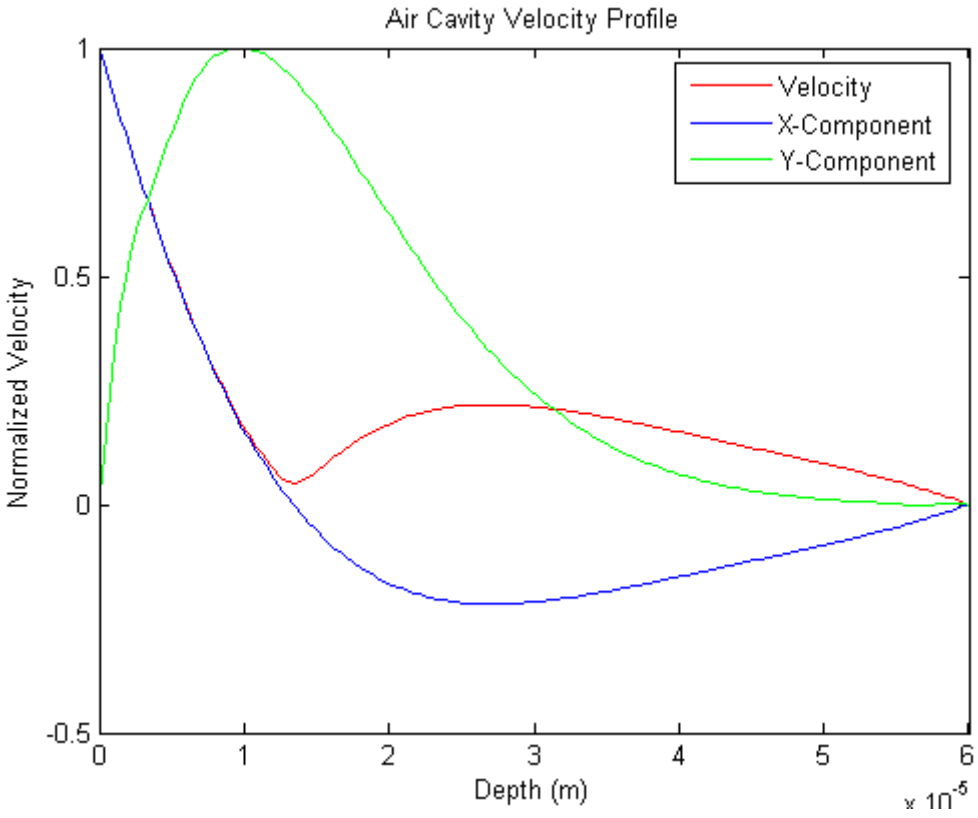

Figure 4.12: Air cavity profile for h*=1

Another key observation is that the cavity penetration depth, or the depth at which the cavity air stops circulating, eventually reaches a terminal value. Therefore for a sufficiently deep cavity, the air recirculation occupies a smaller fraction of the overall channel, leaving the bulk of the channel filled with stationary air. This can be

observed in figure 4.13 where the channel is filled with static air (dark blue) after a sufficient depth.

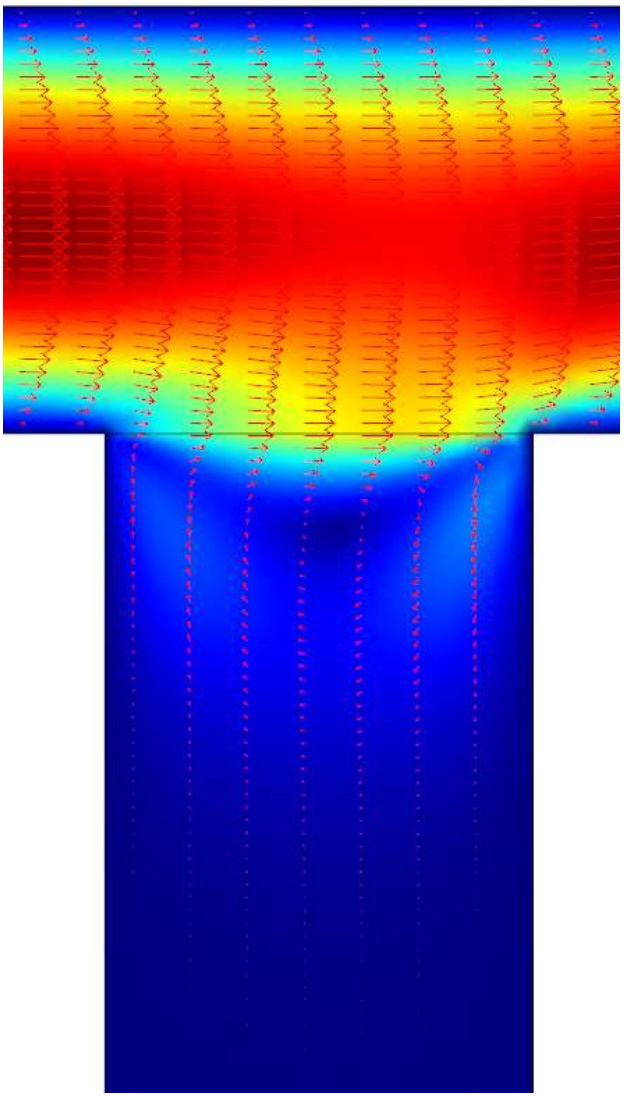

Figure 4.13: Limited air recirculation depth (light blue)

The air-cavity penetration length can be measured by using COMSOL post-processing and measuring the depth in which the air velocity magnitude decays to

1% of u_{slip}. A plot of the penetration depths normalized by the total channel height is show in figure 4.14, as a function of h*.

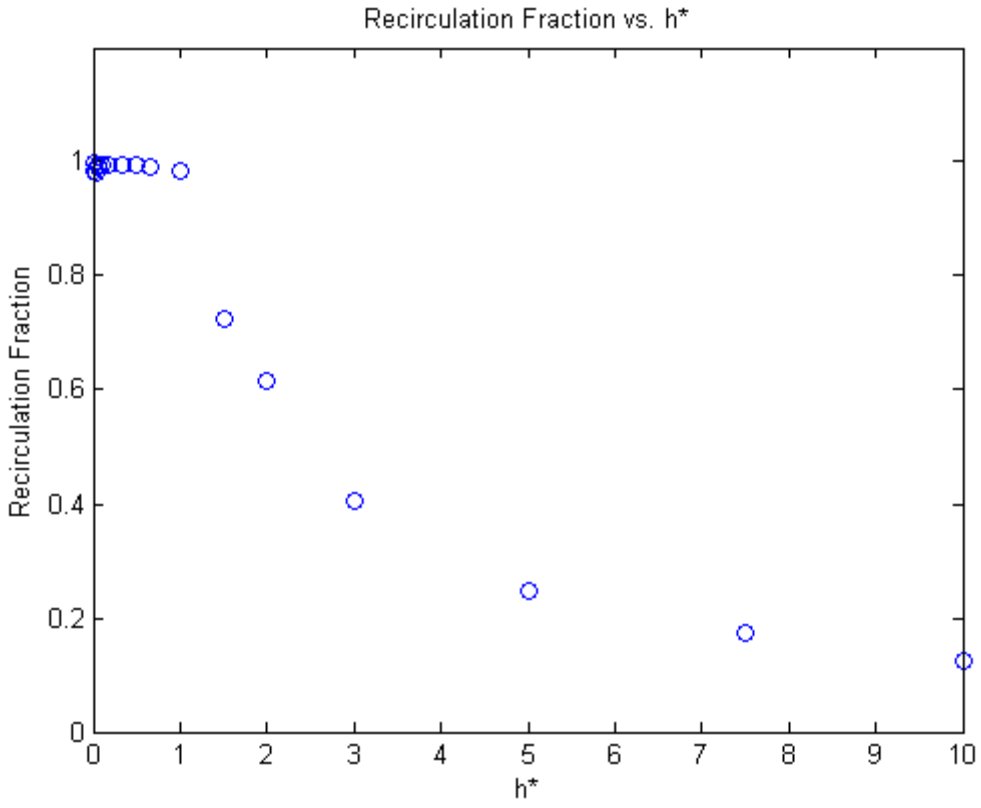

Figure 4.14: Recirculation depth vs h*

At low h* values the recirculation depth or recirculation flow takes up the entire cavity and there is very little decay until the no-slip boundary on the bottom wall is reached. However at higher h* values, specifically past unity, the penetration depth only accounts for a small fraction of the overall cavity (visually seen in figure 4.12). Another way to view the recirculation depth is to normalize them by a fixed

value, such as the water channel height and then plot them against h*, as seen in figure 4.14.

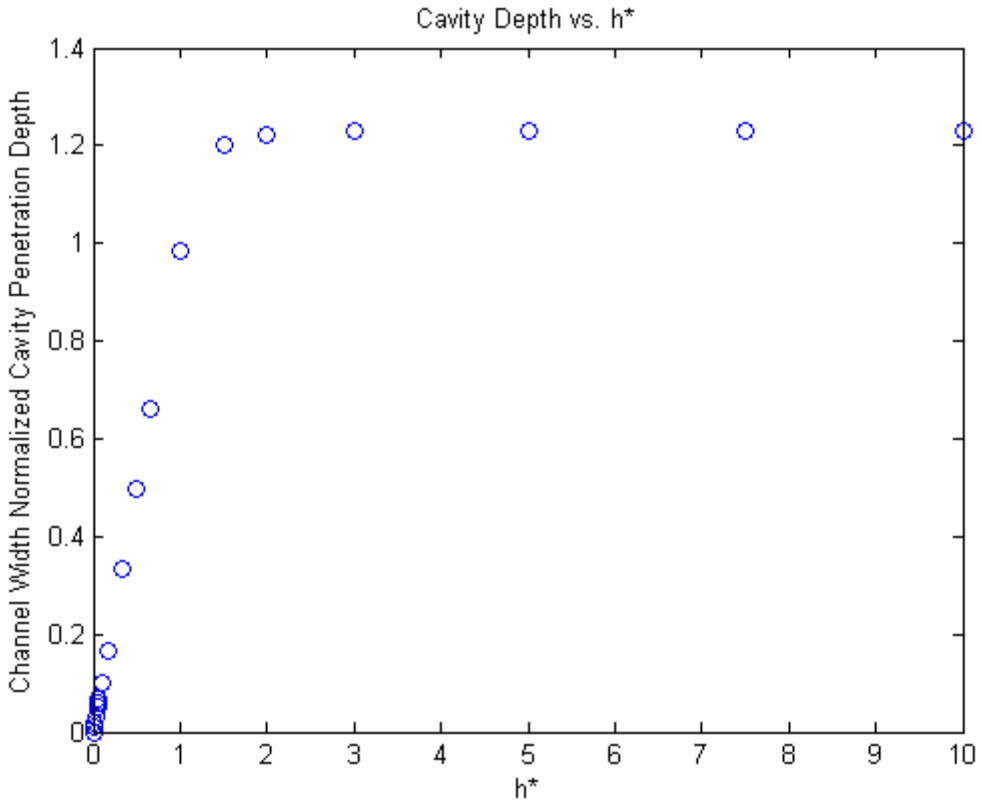

Figure 4.14: Recirculation depth vs h*

From this plot it is apparent that as the air thickness or h* values increases, the recirculation depth approaches an asymptotic value--reminiscent of the asymptotic slip velocity and Q* observed in the Enright and COMSOL model. This is no coincidence--it was previously shown in Chapter 2 that the flow-rate and hence Q* is a function of the slip velocity. Figure 4.15 reinforces this point and shows the normalized slip velocity versus h*.

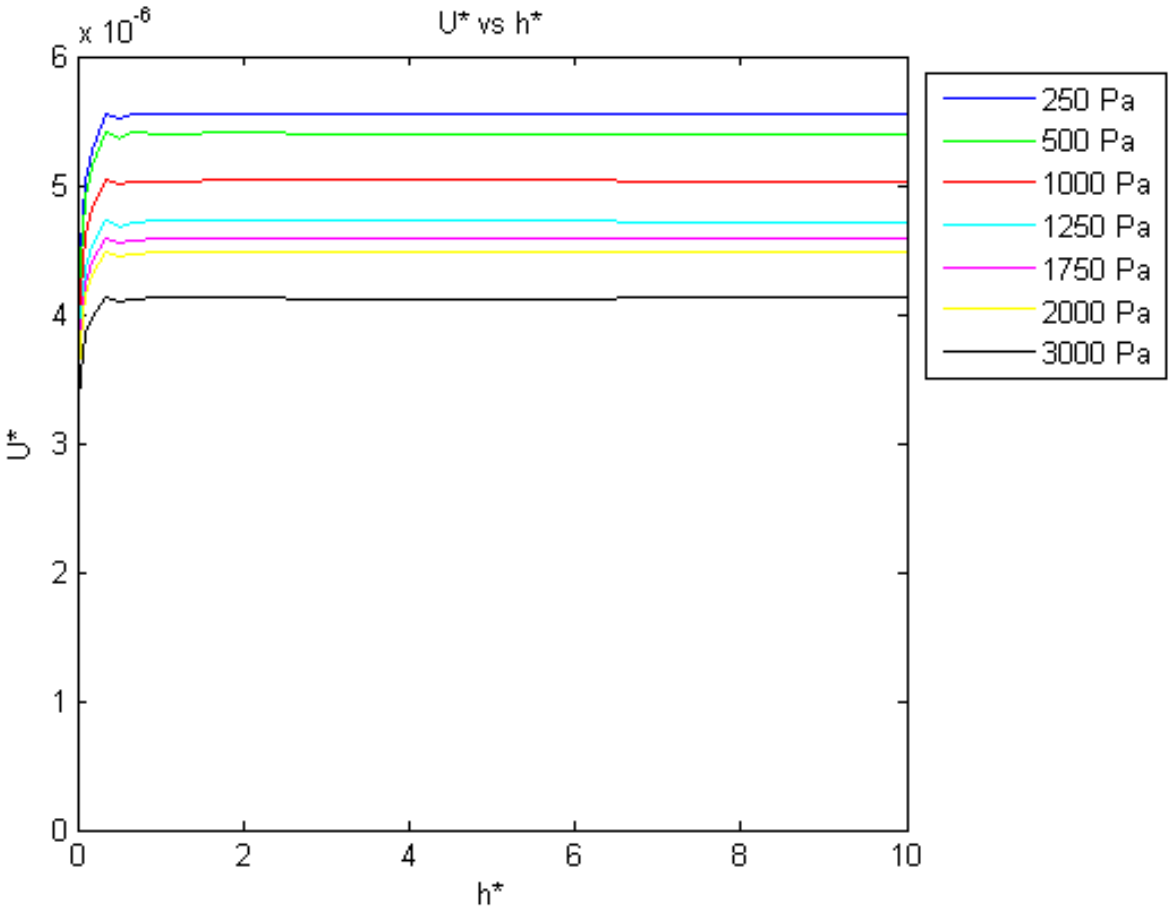

Figure 4.15: Normalized slip velocity vs. h*

Once again a pressure spread exists due to the entrance effects discussed in the previous sections. The non-dimensional U* exhibits the same asymptotic limit observed at high h* values. Furthermore by(0.5), the slip velocity can be related to the slip length construct, as plotted against h* in the following figure.

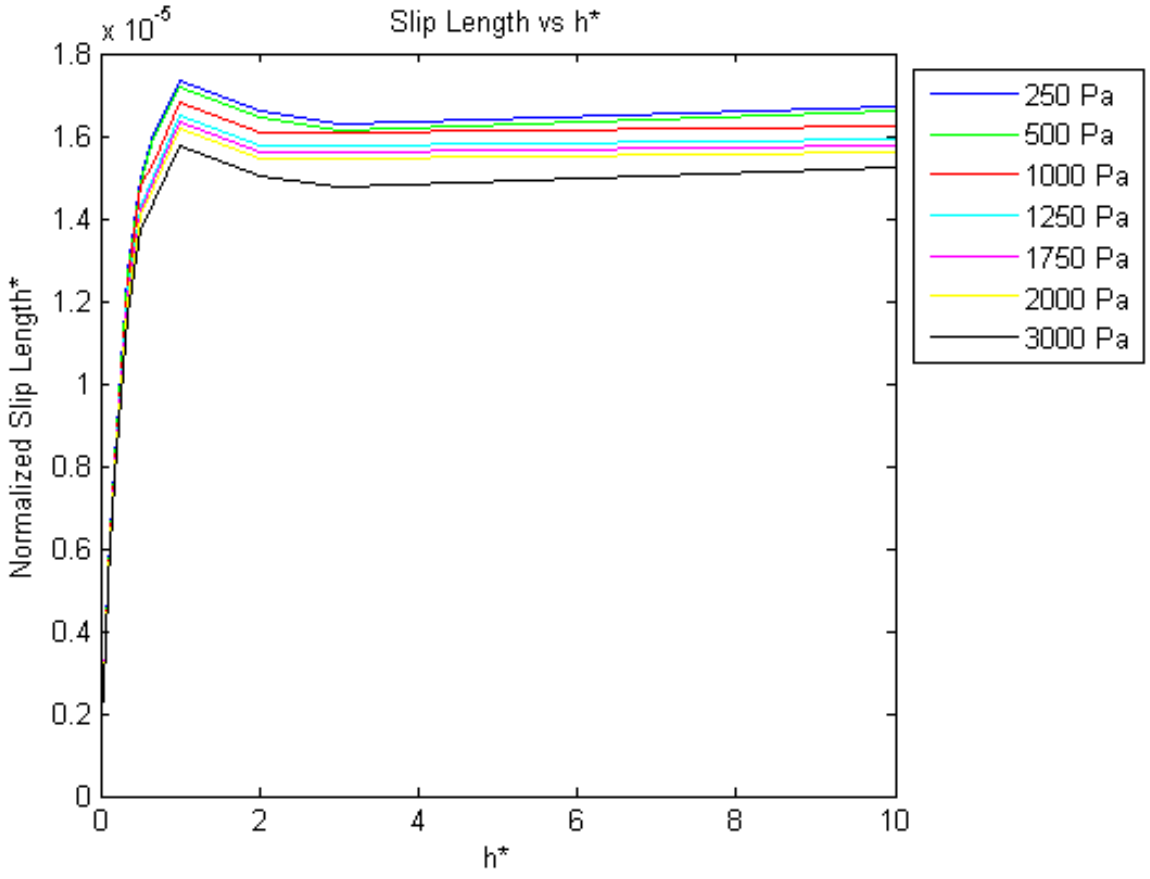

Figure 4.16: Normalized slip length vs. h*

The same plateauing phenomena is observed at high h* values, which can now be related back to the slip velocity in figure 4.15 and recirculation depth in figure 4.14. The recirculation depth can be likened to the fluid depth in which there is an active or finite air velocity, which increases and then plateaus with h*. The recirculation flows are related to the interfacial slip velocity and hence as the slip velocity increases, so does the magnitude of the flow. However as seen in figure 4.12, the

interfacial slip velocity is met with an opposing recirculation of air due to the surface roughness elements and is thus constrained. Furthermore, since the air cavity recirculation penetration reaches a terminal limit as the depth or h* increases, the slip velocity (as seen in figure h*) and by extension slip length (figure 4.16) reach an asymptotic limit. Finally, the overall flow-rate is driven by Navier slip flow and as the recirculated constrained slip velocity reaches an asymptote, it is expected that Q* follows the same trend, as seen originally in figure 4.5.

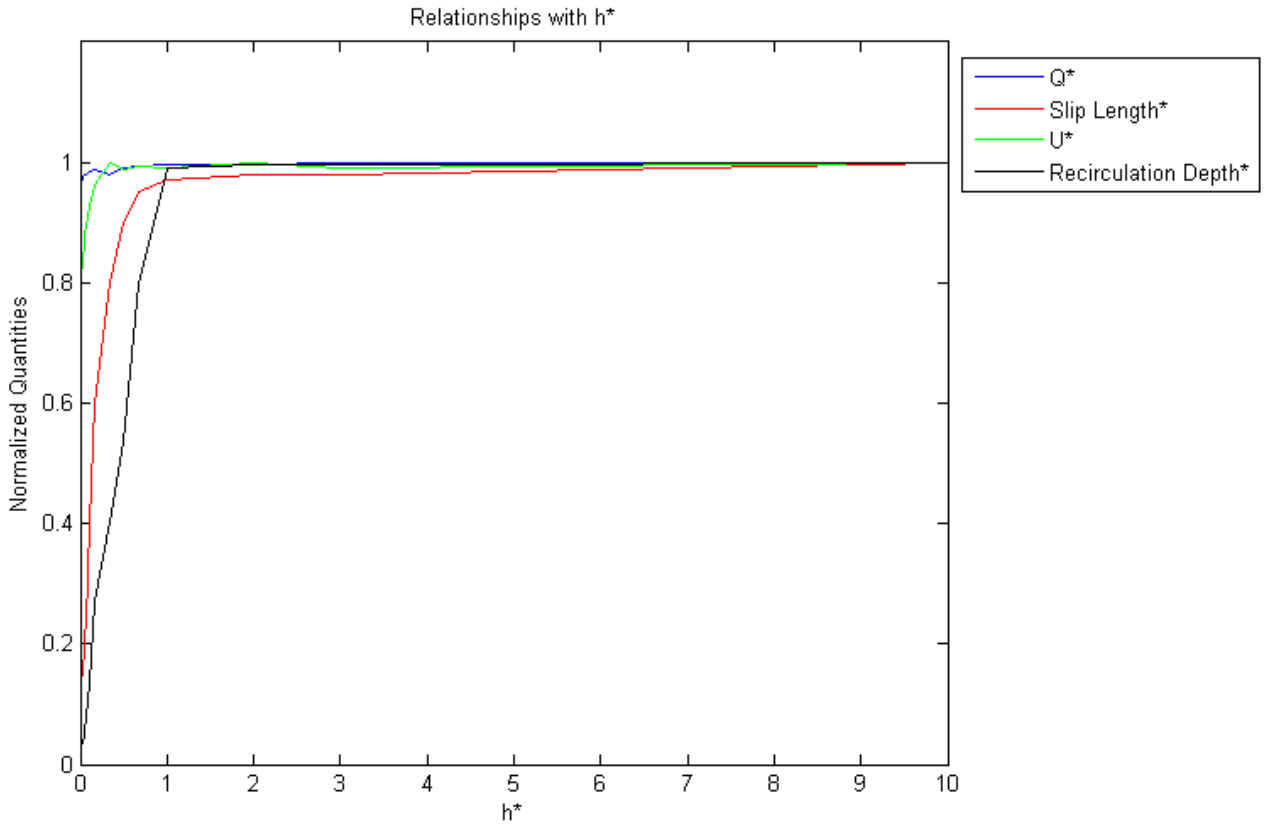

Figure 4.17: Combined plot showing normalized quantities vs. h*

Figure 4.17 depicts normalized quantities of Q*, u*, slip length and the recirculation depth as a function of h* and summarizes the previously stated relationship. The plateauing of the recirculation depth adversely related slip velocity are responsible for the terminal effect seen in the Enright and simulated model. It is now apparent that the effects of the end wall are the major driving factor behind the asymptotic behavior that Enright model depicted.

4.8 END EFFECTS AND ASPECT RATIO

The previous section shed new light upon the flow-rate terminal phenomena in the Enright and COMSOL simulated case. However, the fundamental purpose of superhydrophobic microchannels is to flow a working fluid and hence a flow-rate comparison is necessary. Figure 4.18 compares the Q* values from the Enright case and the COMSOL simulation in which the wall separation distance was fixed at 60 microns. Both Q* trends have the same asymptotic limit that was described before.

Recalling that Q* is an analog for friction factor, figure 4.18 shows that the Enright model predicts higher sustainable flow-rates and hence higher frictional reduction than the 60 micron case. Specifically, the Enright model predicts a 3 times higher flow-rate across the gamut of h* value when compared to the fixed case. However one previously mentioned difference between the two cases is that the Enright model assumes a very large separation distance between the walls. Joshi provided computational evidence that when surface roughness element spacing is increased beyond a critical value, the air-water interface can break down and water will penetrate the cavity [2]. Experimental evidence has also indicated that pillar

spacing is a key parameter in preventing Cassie-Baxter to Wenzel transition [21, 47, 48]. Therefore Enright's basis of extreme separation might not be indicative of states in which the Cassie-Baxter state exists, eliminating the advantages of using superhydrophobic materials.

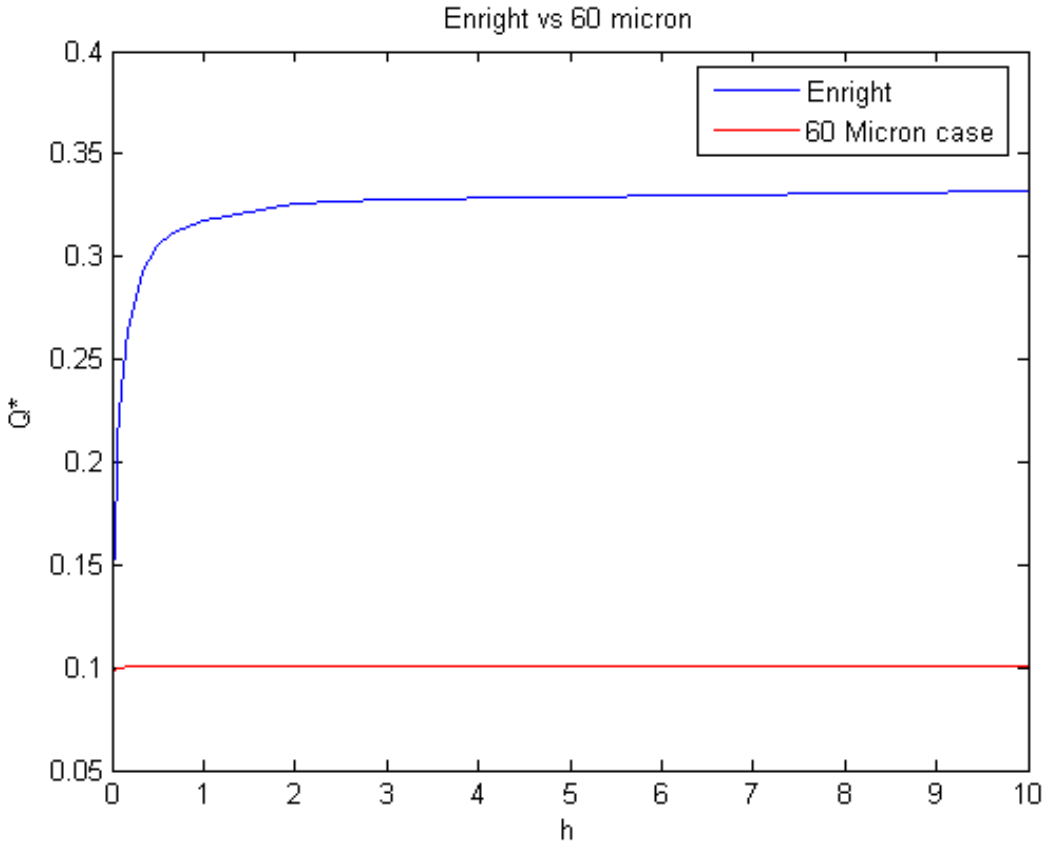

Figure 4.18: Enright versus 60 micron case Q*

Recalling that h* value parameterizes the channel height and air layer ratio, it is necessary to run additional simulations on geometries with variable wall separation in order to see the effect of aspect ratio has on the flow. The author ran simulations on geometries with a wall separation of 30 micron and 90 microns. Given that the

water channel portion of the microchannel, as seen in figure 4.1, is a constant 60 microns, the additional simulations provide insight on cases in which the wall separations are 50% and 150% of the channel.

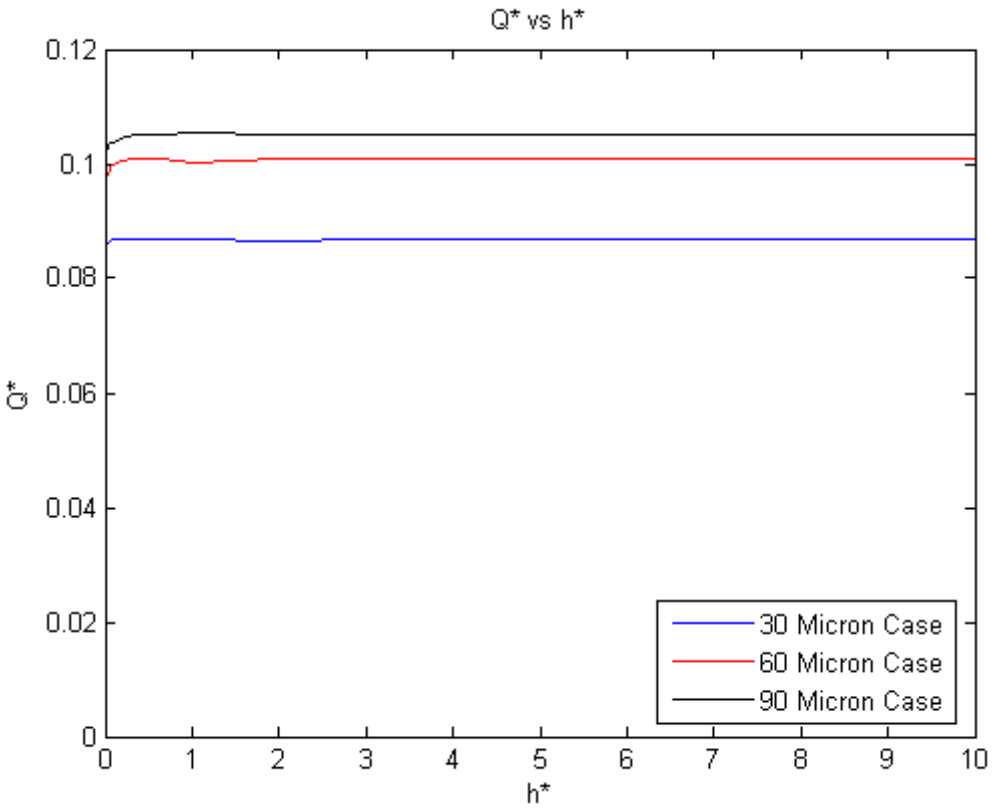

Figure 4.19: Variable spacing Q* comparisons

The results of these simulations are depicted in the above figure 4.19. The 3000 Pascal inlet values were used--as previously discussed, pressure spreads existed within the simulations due to cavity developing effects. All simulated cases show the characteristic asymptotic limit that is a result of recirculation effects. One interesting observation however is that the higher separation spacing cases have a more gradual

transition to a terminal Q*, indicated by a higher degree of concavity at low h* values. This phenomenon can be explained again due to the recirculation caused by the walls. When the wall cavity distance is lowered, the flow length scale is reduced and both the slip-flow and recirculation feel more of the end effects. Once again due to the wall's no-slip condition, a recirculation flow is set up and since the aspect ratio is higher, it will have a more adverse limiting effect on the slip-velocity and hence the flow rate, ultimately leading to convergence at lower h* values. The higher separation cases have lower aspect ratios and wall effects are not felt until higher h* values are reached. It is expected that the higher separation cases have higher Q* values due to higher slip-flow lengths across the microchannel. In summary, as the separation between the wall cavities is lowered, wall effects caused the flow-rate to converge at lower h* values and ultimately results in higher friction and lower flow rate.

Another observation is the asymmetric stratification between the three different separation cases--an increase in separation from 60 microns to 90 microns reduces friction by roughly 5% however a decrease to 30 microns will decrease flow rates by 20%. These results might indicate that the flowing water-layer is starting to approach a fully developed condition.

Figure 4.20 shows an updated comparison of the Enright Q* values and the three spacing configurations.

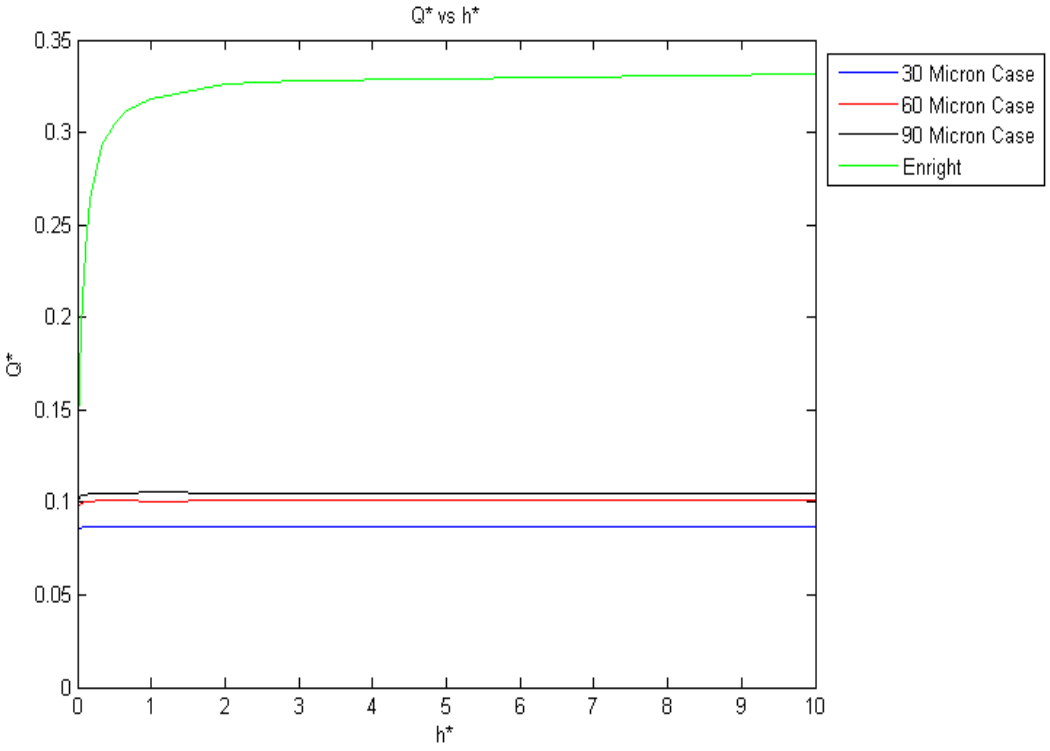

Figure 4.20: Variable spacing and Enright Q* comparisons

The key observation from figure 4.20 is that while a larger separation distance will increase the Q*, it is still apparent that the Enright large separation distance assumption predicts a very large flow rate. Naturally, the Enright profile has more gradual transition at lower h* values due to the absence of wall and end effects. While the other aspect ratios represent a 50% reduction and increase relative to the water channel, the Enright model's higher magnitude Q* indicate a extreme case and might not be realistic for practical applications. The results of the simulation indicate that most experimental microchannels have a much lower frictional reduction than previously predicted by the Kim & Hidrovo and Enright derivation.

Chapter 5: Conclusions and Recommendations

5.1 Overall Comparison and Conclusions

Figure 5.1 below shows a summary of the three different model Q* values as a function of h*.

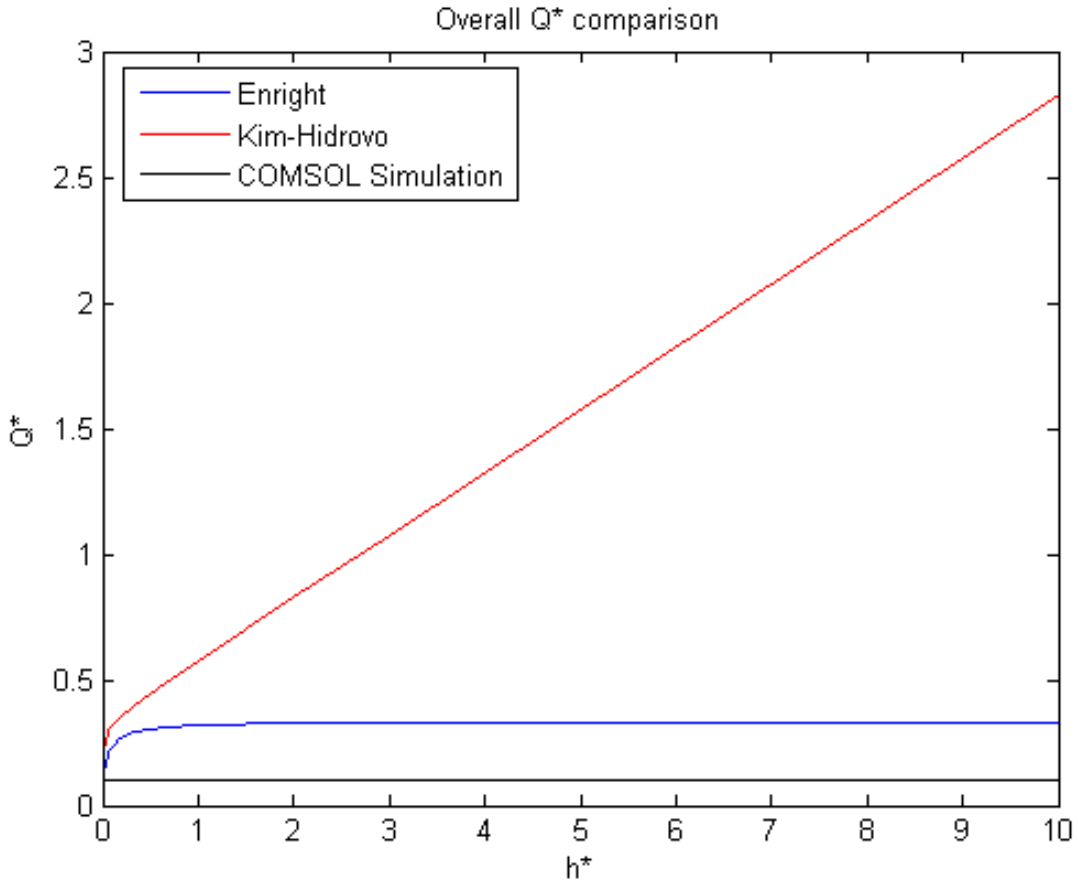

Figure 5.1: Overall comparison of Q*

All models converge to a common Q* of .083 at an h* value of 0 which by (0.39) refers to a Po value of 96, the classical solution for infinite parallel plate flow. The Kim-Hidrovo model predicts a Q* that increases linearly with the air-layer thickness h* and thus claims to have the highest frictional reduction. This is due to the unbounded slip velocity and flow-rate that is a result of a shift from Poiseuille driven water flow to a strongly Couette driven air-layer flow. The Kim-Hidrovo derivation is more applicable to a multiphase slip flow under a common pressure gradient and does not take into account the existence of features which induce recirculation.

Next the Enright case shows a much lower Q* than the Kim-Hidrovo case and has a characteristic plateauing of the Q* at higher h* values. This phenomena has been concluded to be a result of recirculation and end effects that inhibit an unbounded slip-velocity and hence flow-rate. The Enright model assumes a very large separation distance between the walls and thus neglects end effects.

Finally the COMSOL simulations provided in this report focus on microchannels with feature sizes that are typically an order of magnitude of the channel width, a realistic assumption in most experiments. In these cases, the recirculation and wall effects play a much stronger role and inhibit the slip-velocity and cause a lower flow-rate and thus Q* value. The results of these simulations provide a better idealized ceiling for the expected Q* and hence friction factor values that can be observed in superhydrophobic microchannels.

One point that might be of interest is that the new COMSOL model and to a lesser extent the Enright predicts a terminal Q* at low h* values, specifically on

order of 1 or below. This provides evidence that there is a diminishing utility for microchannels to have air-layers greater than unity with respect to the water layer and hence points to design parameters aimed at maximizing flow-rates while minimizing material usage. While microfabrication and lithography techniques [1, 30] have been improving, they are still time consuming and rather expensive. Since a microchannel will only benefit from an air-layer thickness on order of the channel width or lower, the results might be able to form the basis of optimum design for fluid-flow applications.

5.2 LIMITS TO STUDY AND FUTURE RECOMMENDATIONS

While the results of the study provide a new benchmark for design and friction factor values, as well as provide insight into recirculation and wall-effects, there are some limitations. First, the interface was modeled as ideal Cassie-Baxter and therefore was planar and stationary. Real interfaces have a Laplace curvature associated with them which should be accounted for. Next the stability of the Cassie-Baxter is an area of active research and in recent experiments [47-52] it has been observed that under a critical pressure the Cassie-Baxter state can collapse to a Wenzel, or fully water penetrated state. Finally there has been evidence [25, 55] of asymmetric water penetration occurring on particularly deep channels, causing deviations from the idealized behavior. A more rigorous analysis should employ the effects of curvature on the flow-rate and Q* values and possibly transient effects that play a role in the overall flow properties of the superhydrophobic microchannel.

References

1. Shiu, J.Y. and P. Chen, *Addressable protein patterning via switchable superhydrophobic microarrays.* Advanced Functional Materials, 2007. **17**(15): p. 2680-2686.
2. Joshi, S. *Design of Arrayed Micro-Structures to get Super-Hydrophonic Surface for Single Droplet and Bulk Flow Conditions*. in *COMSOL Conference* 2009. Bangalore
3. Carlborg, C.F., et al., *Continuous flow switching by pneumatic actuation of the air lubrication layer on superhydrophobic microchannel walls.* Mems 2008: 21st Ieee International Conference on Micro Electro Mechanical Systems, Technical Digest, 2008: p. 599-602
4. Londe, G., et al., *A passive microfluidic valve using superhydrophobic/hydrophilic nanostructures for Lab-On-a-Chip (LOC) systems.* Transducers '07 & Eurosensors Xxi, Digest of Technical Papers, Vols 1 and 2, 2007: p. U909-U910
5. Vinogradova, O.I., *Slippage of water over hydrophobic surfaces.* International Journal of Mineral Processing, 1999. **56**(1-4): p. 31-60.
6. Watanabe, K., Yanuar, and H. Udagawa, *Drag reduction of Newtonian fluid in a circular pipe with a highly water-repellent wall.* Journal of Fluid Mechanics, 1999. **381**: p. 225-238.
7. Watanabe, K., Yanuar, and H. Mizunuma, *Slip of Newtonian fluids at solid boundary.* Jsme International Journal Series B-Fluids and Thermal Engineering, 1998. **41**(3): p. 525-529.
8. Zhu, Y.X. and S. Granick, *Rate-dependent slip of Newtonian liquid at smooth surfaces.* Physical Review Letters, 2001. **8709**(9): p. art. no.-096105.
9. Tretheway, D.C. and C.D. Meinhart, *Apparent fluid slip at hydrophobic microchannel walls.* Physics of Fluids, 2002. **14**(3): p. L9-L12.
10. Choi, C.H., K.J.A. Westin, and K.S. Breuer, *Apparent slip flows in hydrophilic and hydrophobic microchannels.* Physics of Fluids, 2003. **15**(10): p. 2897-2902.
11. Youngblood, J.P. and T.J. McCarthy, *Ultrahydrophobic polymer surfaces prepared by simultaneous ablation of polypropylene and sputtering of poly(tetrafluoroethylene) using radio frequency plasma.* Abstracts of Papers of the American Chemical Society, 1999. **218**: p. U408-U408.
12. Barthlott, W. and C. Neinhuis, *Purity of the sacred lotus, or escape from contamination in biological surfaces.* Planta, 1997. **202**(1): p. 1-8.
13. Kim, J.W. and C.J. Kim, *Nanostructured surfaces for dramatic reduction of flow resistance in droplet-based microfluidics.* Fifteenth Ieee International Conference on Micro Electro Mechanical Systems, Technical Digest, 2002: p. 479-482
14. Lauga, E. and H.A. Stone, *Effective slip in pressure-driven Stokes flow.* Journal of Fluid Mechanics, 2003. **489**: p. 55-77.

15. Min, T.G. and J. Kim, *Effects of hydrophobic surface on skin-friction drag.* Physics of Fluids, 2004. **16**(7): p. L55-L58.
16. Gogte, S., et al., *Effective slip on textured superhydrophobic surfaces.* Physics of Fluids, 2005. **17**(5): p. -.
17. Truesdell, R., et al., *Drag reduction on a patterned superhydrophobic surface.* Physical Review Letters, 2006. **97**(4): p. -.
18. Ou, J., B. Perot, and J.P. Rothstein, *Laminar drag reduction in microchannels using ultrahydrophobic surfaces.* Physics of Fluids, 2004. **16**(12): p. 4635-4643.
19. Ou, J. and J.P. Rothstein, *Direct velocity measurements of the flow past drag-reducing ultrahydrophobic surfaces.* Physics of Fluids, 2005. **17**(10): p. -.
20. Choi, C.H., et al., *Effective slip and friction reduction in nanograted superhydrophobic microchannels.* Physics of Fluids, 2006. **18**(8): p. -.
21. Byun, D., J. Kim, and J. Hong, *Slippage and Wetting Transition of Water Flow in Superhydrophobic Micro-Channel.* Proceedings of the 6th International Conference on Nanochannels, Microchannels, and Minichannels, Pts a and B, 2008: p. 1229-1235
22. Wang, S. and L. Jiang, *Definition of superhydrophobic states.* Advanced Materials, 2007. **19**(21): p. 3423-3424.
23. Kim, T.J., *Superhydrophobic friction reduction microtextured surfaces* in *ASME Micro/Nanoscale Heat & Mass Transfer International Conference*. 2009: Shanghai
24. Enright, R., et al., *Friction factors and Nusselt numbers in microchannels with superhydrophobic walls.* Proceedings of the 4th International Conference on Nanochannels, Microchannnels, and Minichannels, Pts A and B, 2006: p. 599-609
25. Byun, D., et al., *Direct measurement of slip flows in superhydrophobic microchannels with transverse grooves.* Physics of Fluids, 2008. **20**(11): p. -.
26. Maynes, D., et al., *Laminar flow in a microchannel with hydrophobic surface patterned microribs oriented parallel to the flow direction.* Physics of Fluids, 2007. **19**(9): p. -.
27. Lee, C., C.H. Choi, and C.J. Kim, *Structured surfaces for a giant liquid slip.* Physical Review Letters, 2008. **101**(6): p. -.
28. Hao, P.F., et al., *Laminar Drag Reduction in Hydrophobic Microchannels.* Chemical Engineering & Technology, 2009. **32**(6): p. 912-918.
29. Shirtcliffe, N.J., et al., *Superhydrophobic Copper Tubes with Possible Flow Enhancement and Drag Reduction.* Acs Applied Materials & Interfaces, 2009. **1**(6): p. 1316-1323.
30. Zhou, Y.L., et al., *Superhydrophobic surface created by the silver mirror reaction and its drag-reduction effect on water.* Journal of Materials Chemistry, 2009. **19**(20): p. 3301-3306.
31. Barrat, J.L. and L. Bocquet, *Large slip effect at a nonwetting fluid-solid interface.* Physical Review Letters, 1999. **82**(23): p. 4671-4674.

32. Cieplak, M., J. Koplik, and J.R. Banavar, *Boundary conditions at a fluid-solid interface.* Physical Review Letters, 2001. **86**(5): p. 803-806.
33. Thompson, P.A. and S.M. Troian, *A general boundary condition for liquid flow at solid surfaces.* Nature, 1997. **389**(6649): p. 360-362.
34. Barat, J.-L., *Dynamics of simple liquids at heterogenous surfaces: Molecular-dynamics simulations and hydrodynamic description.* European Physical Journal E, 2004(15): p. 427-438.
35. Kandlikar, S.G., et al., *Characterization of surface roughness effects on pressure drop in single-phase flow in minichannels.* Physics of Fluids, 2005. **17**(10): p. -.
36. Salamon, T., et al., *Numerical simulation of fluid flow in microchannels with superhydrophobic walls.* Proceedings of the ASME Heat Transfer Division 2005, Vol 1, 2005. **376-1**: p. 819-829
37. Nie, X.B., G.D. Doolen, and S.Y. Chen, *Lattice-Boltzmann simulations of fluid flows in MEMS.* Journal of Statistical Physics, 2002. **107**(1-2): p. 279-289.
38. Rawool, A.S., S.K. Mitra, and S.G. Kandlikar, *Numerical simulation of flow through microchannels with designed roughness.* Microfluidics and Nanofluidics, 2006. **2**(3): p. 215-221.
39. Dupuis, A., E.M. Kotsalis, and P. Koumoutsakos, *Coupling lattice Boltzmann and molecular dynamics models for dense fluids.* Physical Review E, 2007. **75**(4): p. -.
40. El-Genk, M.S. and I.H. Yang, *Numerical analysis of laminar flow in micro-tubes with a slip boundary.* Energy Conversion and Management, 2009. **50**(6): p. 1481-1490.
41. Sedighi, N., S. Murad, and S.K. Aggarwal, *Molecular dynamics simulations of nanodroplet wetting on a solid surface.* Atomization and Sprays, 2009. **19**(2): p. 191-205.
42. Daniello, R.J., N.E. Waterhouse, and J.P. Rothstein, *Drag reduction in turbulent flows over superhydrophobic surfaces.* Physics of Fluids, 2009. **21**(8): p. -.
43. Joshi, Y. *METL Georgie Institute of Technology* 2010 [cited; Available from: http://www.me.gatech.edu/METTL/.
44. Young, T., *An Essay on the Cohesion of Fluids* Philosophical Transactions of the Royal Society, 1805(85): p. 65-87.
45. Wenzel, R., *Resistance of Solid Surfaces to Wetting by Water.* Industrial and Engineering Chemistry 1936. **28**(8): p. 998-994.
46. Cassie, A., *Wettability of Porous Surfaces* Faraday Transactions, 1944(40): p. 546-551.
47. Bormashenko, E., et al., *Cassie-wenzel wetting transition in vibrating drops deposited on rough surfaces: Is the dynamic cassie-wenzel wetting transition a 2D or 1D affair?* Langmuir, 2007. **23**(12): p. 6501-6503.
48. Bahadur, V. and S.V. Garimella, *Preventing the Cassie-Wenzel Transition Using Surfaces with Noncommunicating Roughness Elements.* Langmuir, 2009. **25**(8): p. 4815-4820.

49. Koishi, T., et al., *Coexistence and transition between Cassie and Wenzel state on pillared hydrophobic surface.* Proceedings of the National Academy of Sciences of the United States of America, 2009. **106**(21): p. 8435-8440.
50. Peters, A.M., et al., *Cassie-Baxter to Wenzel state wetting transition: Scaling of the front velocity.* European Physical Journal E, 2009. **29**(4): p. 391-397.
51. Bormashenko, E., *Why does the Cassie-Baxter equation apply?* Colloids and Surfaces a-Physicochemical and Engineering Aspects, 2008. **324**(1-3): p. 47-50.
52. Vrancken, R.J., et al., *Fully Reversible Transition from Wenzel to Cassie-Baxter States on Corrugated Superhydrophobic Surfaces.* Langmuir, 2010. **26**(5): p. 3335-3341.
53. Philip, J.R., *Integral Properties of Flows Satisfying Mixed No-Slip and No-Shear Conditions.* Zeitschrift Fur Angewandte Mathematik Und Physik, 1972. **23**(6): p. 960-968.
54. Bejan, A., *Convection heat transfer*. 3rd ed. 2004, Hoboken, N.J.: Wiley. xxxi, 694 p.
55. Enright, R., et al., *Effects of Interfacial Position on Drag Reduction in a Superhydrophobic Microchannel.* Proceedings of the 6th International Conference on Nanochannels, Microchannels, and Minichannels, Pts a and B, 2008: p. 835-845

Vita

Neil P. Shah was born in Houston, Texas and graduated from William P. Clements High School. Neil originally enrolled at the University of Houston but transferred after his freshman year to The University of Texas at Austin, where he ultimately graduated in 2008 with a Bachelor of Science in Mechanical Engineering. As an undergraduate, Neil researched with Dr. Schenider from the Nuclear and Radiation Engineering program and also spent his summers working within the oil & gas industry. After graduation, Neil decided to stay at The University of Texas at Austin for graduate studies.

Permanent address: 7019 Dunbarton
Sugar Land, TX 77479
Email: nshah0617@gmail.com

This report was typed by Neil P Shah.